

Robust and tunable signal processing in mammalian cells via engineered covalent modification cycles

Ross D. Jones^{1,2}, Yili Qian^{2,3}, Katherine Ilija^{1,2}, Benjamin Wang^{2,4}, Michael T. Laub^{2,4,5},
Domitilla Del Vecchio^{*2,3}, and Ron Weiss^{*1,2,6}

¹Department of Biological Engineering, Massachusetts Institute of Technology, Cambridge, MA, 02139, USA.

²Synthetic Biology Center, Massachusetts Institute of Technology, Cambridge, MA, 02139, USA.

³Department of Mechanical Engineering, Massachusetts Institute of Technology, Cambridge, MA, 02139, USA.

⁴Department of Biology, Massachusetts Institute of Technology, Cambridge, MA, 02139, USA.

⁵Howard Hughes Medical Institute, Massachusetts Institute of Technology, Cambridge, MA, 02139, USA.

⁶Electrical Engineering and Computer Science Department, Massachusetts Institute of Technology, Cambridge, MA, 02139, USA.

*Correspondence should be addressed to D.D.V. (ddv@mit.edu). or R.W. (rweiss@mit.edu)

Abstract

Rewired and synthetic signaling networks can impart cells with new functionalities and enable efforts in engineering cell therapies and directing cell development. However, there is a need for tools to build synthetic signaling networks that are tunable, can precisely regulate target gene expression, and are robust to perturbations within the complex context of mammalian cells. Here, we develop synthetic phosphorylation-based and feedback-controlled devices with such properties in mammalian cells using proteins derived from bacterial two-component signaling pathways. First, we isolate kinase and phosphatase proteins from the bifunctional histidine kinase EnvZ. We then use these enzymes to engineer a synthetic covalent modification cycle, in which the kinase and phosphatase competitively regulate phosphorylation of the cognate response regulator OmpR, enabling analog tuning of OmpR-driven gene expression. Further, we show that the phosphorylation cycle can be extended by connecting phosphatase expression to small molecule and miRNA inputs in the cell, with the latter enabling cell-type specific signaling responses and accurate cell type classification. Finally, we implement a tunable negative feedback controller by co-expressing the kinase-driven output gene with the small molecule-tunable phosphatase. This negative feedback substantially reduces cell-to-cell noise in output expression and mitigates the effects of cell context perturbations due to off-target regulation and resource competition. Our work thus lays the foundation for

establishing tunable, precise, and robust control over cell behavior with synthetic signaling networks.

1 Introduction

Across all organisms, sensing and processing of environmental factors is critical for growth, proliferation, and survival¹. Engineering of mammalian cells to transmute specific intracellular and extracellular inputs into desirable output behaviors has broad applications in cell therapy, biomanufacturing and the engineering of stem cells, tissues, and organoids²⁻⁸. Recently, work has accelerated to rewire natural signaling pathways and engineer synthetic receptors that sense extracellular inputs^{9,10}. A desirable engineered signaling system would have tunable input/output responses, low output noise, and drive gene expression that is robust to perturbations coming from the extracellular, cellular, and genetic context of the system¹¹. The ability of the signaling system to exhibit such properties depends on how input signals are processed to generate gene expression outputs. However, relatively little work has been done to engineer such signal processing behavior in mammalian cells.

To date, nearly all engineered signaling systems have utilized either native intracellular signaling domains or proteolytic mechanisms to transduce extracellular signals into intracellular responses¹⁰. Interfacing with the cell's natural signaling networks has been a powerful method to rewire signaling pathways¹⁰, but it is difficult to modulate signaling between natural receptors and their gene expression targets due to the complexity of natural signaling networks in mammalian cells. Alternatively, using proteolysis to liberate gene regulators from the plasma membrane enables regulation independent from the cell signaling context through non-native proteins such as dCas9 or tTA¹⁰. However, because the effector proteins are irreversibly released from the receptor and thus the signaling system cannot be easily reset to its initial state, the ability to tune the input-output response is limited. Recently, synthetic receptors comprising extracellular receptors or dimerization domains fused to a bacterial two-component signaling (TCS) protein were shown to successfully transmute extracellular ligand inputs to TCS-regulated transcriptional outputs in mammalian cells^{12,13}.

The use of TCS proteins in synthetic mammalian signaling networks has the potential for creating tunable, robust signaling circuits that do not cross-react with existing networks in mammalian cells. TCS pathways are ubiquitous in bacteria, but are generally rare in eukaryotes and absent in animals¹⁴. TCS pathways typically comprise a transmembrane sensor protein called a histidine kinase (HK) and a cognate intracellular effector protein called a response regulator (RR). In response to specific signal inputs, the HK autophosphorylates on a conserved histidine residue and then transfers the phosphoryl group to a conserved aspartate residue in the receiver (Rec) domain of the RR (referred to as the HK's kinase activity). Once phosphorylated, most RRs carry out transcriptional regulation, though other modes of regulation are possible^{15,16}. Unlike typical eukaryotic receptors, in the absence of signal inputs, most HKs catalyze removal of the phosphoryl group from their cognate RRs (referred to as the HK's phosphatase activity)^{16,17}. The presence of signal input alters the conformational state of the HK, thereby tuning its relative kinase and phosphatase activities¹⁸. The bifunctional nature of HKs is important for insulating TCS pathways

33 from off-target interactions^{19,20} as well as for increasing the responsiveness to signal inputs²¹. The recently developed
34 TCS-based receptors work by coupling ligand-induced dimerization of the receptor to HK kinase activity and thus
35 RR-driven gene expression^{12,13}. The lack of any known examples of histidine-aspartate phosphorelays in mammalian
36 cells strongly suggests that these introduced TCS signaling pathways are insulated from mammalian signaling
37 pathways^{12,13,22}.

38 Here, we introduce a framework for engineering signal processing circuits in mammalian cells based on synthetic
39 covalent modification cycles (CMCs) built with bacterial TCS proteins (Figure 1). In phosphorylation cascades,
40 phosphatases that are constitutively active or part of a negative feedback loop can impart tunability and robustness to
41 perturbations into the system through the reversal of substrate phosphorylation^{23–27}. To develop such circuits, we
42 isolate monofunctional kinases and phosphatases from the bifunctional *E. coli* HK EnvZ²⁸, then use specific
43 phosphorylation and dephosphorylation of EnvZ's cognate RR OmpR to regulate downstream gene expression via
44 transcriptional activation. First, we illustrate the tunability of this system by using the level of an EnvZ phosphatase
45 to shift the sensitivity of OmpR-driven gene expression output to the levels of an EnvZ kinase. Further, we show that
46 kinase-to-output dose responses can be tuned by regulating phosphatase expression with small molecule-inducible
47 degradation domains. We then build upon this tunability to create novel phosphorylation-based miRNA sensors that
48 are capable of cell type classification and enable cell-type specific tuning of signaling responses.

49 A major challenge for developing synthetic genetic circuits is undesirable context-dependence due to factors such
50 as off-target binding of gene regulators and overloading of cellular factors used in gene expression (*i.e.* resources),
51 which can perturb gene expression levels^{29,30}. Currently, there is a lack of synthetic signaling circuits that are robust
52 to such context effects in mammalian cells. To address this problem, we introduced robustness to perturbations into
53 the kinase-to-output process via negative feedback control. The negative feedback is achieved by co-expressing the
54 output protein with a phosphatase that dephosphorylates OmpR, returning it to an inactive form. The feedback
55 strength and output level can be tuned via a small molecule-inducible degradation domain fused to the phosphatase.
56 The addition of feedback control substantially reduces cell-to-cell noise in output expression and mitigates the effects
57 of off-target translational repression and transcriptional resource loading on the signaling input-output response.
58 Overall, we present the design and characterization of phosphorylation-regulated genetic modules that enables
59 tunable, precise, and robust control of signaling outputs in mammalian cells.

60 **2 Results**

61 62 **2.1 Engineering EnvZ to isolate kinase and phosphatase activity**

63 As a model system for engineering synthetic signal processing circuits, we utilized the well-characterized
64 EnvZ-OmpR TCS pathway from *E. coli*³¹. Like many HKs, EnvZ is bifunctional, actuating both kinase and
65 phosphatase activity onto its cognate RR OmpR²⁸. We thus reasoned that we could isolate the individual kinase and
66 phosphatase activities of EnvZ to generate enzymes suitable for implementing a CMC. In particular, we expected that
67 by starting with a bifunctional enzyme, we could selectively mutate or otherwise disrupt the kinase or phosphatase
68 activity of EnvZ, yielding an enzyme significantly biased towards one activity or the other (Figure 2a). Both *in vitro*
69 and *in vivo* in bacteria, it has been shown that this objective can be achieved through various mutations³²⁻³⁴,
70 truncations^{35,36}, and domain rearrangements³⁷. In mammalian cells, it was shown that wild-type (WT) EnvZ is
71 constitutively active²², indicating that it has net-kinase activity, but may still retain some phosphatase activity and
72 thus not operate as potently as a pure kinase. To begin creating more monofunctional kinases and phosphatases from
73 EnvZ in mammalian cells, we generated several variants of EnvZ using established mutations, truncations, domain
74 rearrangements, and novel combinations thereof (Figure 2b-d).

75 To test for kinase activity, we evaluated the ability of EnvZ variants to activate an OmpR-driven reporter when
76 transfected into HEK-293FT cells (Figure 2e, left). OmpR-activated promoters were made by placing three to nine
77 OmpR binding sites upstream of a minimal CMV promoter or a synthetic minimal promoter (YB_TATA²², referred
78 to as minKB), of which the 6xOmpR_{BS}-minCMV variant was chosen for use in most downstream experiments due to
79 its high fold-change in response to OmpR phosphorylation (Supplementary Figure 1). From this initial screen, we
80 identified two variants, EnvZm2 [T247A] and EnvZm2[AAB], the latter having an extra DHP domain fused to
81 EnvZ[223+]³⁷, that induced higher levels of output expression than WT EnvZ, suggesting that their phosphatase
82 activity is reduced (Figure 2e, right; see Supplementary Figure 2 for further experimental details and data analysis).
83 Variants expected to be deficient in ATP binding or autophosphorylation based on previous studies in bacteria were
84 indeed found to lack activation of OmpR-VP64, indicating that in mammalian cells they also lack kinase activity
85 (Figure 2e, right). Moving forward, we used EnvZm2 as our kinase of choice due to its improvement in kinase
86 activity and the highly conserved ability of the T247A mutation to reduce or eliminate phosphatase activity in other
87 HKs^{38,39}.

88 To test for phosphatase activity, we co-expressed EnvZm2 with OmpR-VP64 to generate phosphorylated
89 OmpR-VP64 (P-OmpR-VP64), and then evaluated the ability of our EnvZ variants to deactivate expression of an
90 OmpR-driven reporter (Supplementary Figure 3f, left). While several EnvZ variants predicted to be phosphatases
91 based on previous studies indeed showed deactivation of OmpR-driven expression at high concentrations, this
92 deactivation was comparable to that of a variant predicted to lack any catalytic activity (EnvZm0m1m2m3
93 [H243A/D244A/T247A/N343K]) (Figure 2f, right; & Supplementary Figure 3). Thus, it is possible that these
94 variants were primarily inhibiting output expression through sequestration of P-OmpR-VP64 from its target
95 promoter, rather than through dephosphorylation. Indeed, high dosages of such a variant (EnvZm1, [T247A]) can

96 reduce "leaky" activation of the output reporter by non-phosphorylated OmpR-VP64, indicating that the observed
97 reduction in output can occur absent dephosphorylation (Supplementary Figure 4). Notably, at both low (Figure 2f)
98 and high (Supplementary Figure 4) dosages of the variant EnvZ[A] (DHP domain only), we found no apparent
99 phosphatase activity, contrasting with the original report³⁶. Only variant EnvZm1[AAB], having an extra DHP
100 domain fused to EnvZ[223+] with the mutation [D244A] in both DHP domains, was found to deactivate
101 OmpR-driven expression more strongly than EnvZm0m1m2m3 (which lacks catalytic activity) (Figure 2f, far-right),
102 suggesting EnvZm1[AAB] has phosphatase activity in mammalian cells. However, at higher dosages of
103 EnvZm1[AAB] and in the absence of EnvZm2, OmpR-VP64 appears to become activated, indicating that this variant
104 may still retain some kinase activity (Supplementary Figure 4). We thus sought another means to generate a strong
105 EnvZ phosphatase that is functional in mammalian cells.

106 **2.2 Derivation of strong EnvZ phosphatases through DHP domain rotations**

107 Because of the constitutive kinase activity of WT EnvZ and the lack of clear monofunctional phosphatase activity
108 by purported phosphatase variants of EnvZ, we hypothesized that in mammalian cells, EnvZ may take a structural
109 conformation that is unfavorable for phosphatase activity. Previously, it was shown that the capability for
110 autophosphorylation by the HK AgrC can be modulated through changing the rotational state of the DHP domain⁴⁰.
111 We hypothesized that this rotational conformation may also affect access to the phosphatase state. We therefore
112 followed the approach of Wang *et al.*⁴⁰ to force the alpha helices in the DHP domain of EnvZ into fixed rotational
113 states using GCN4 leucine zippers (Figure 3a).

114 We generated a library of 10 rotationally-locked variants (EnvZt#1-10) with and without a mutation to eliminate
115 ATP binding and hence kinase activity (m3 – [N343A])³³. As expected, we observed a range of OmpR-driven gene
116 expression levels that depend on the putative rotational angle of the DHP domain (Figure 3b-c). Interestingly,
117 compared to WT EnvZ, all of the EnvZt# variants drove equivalent or weaker output activation by OmpR-VP64,
118 while also reducing EnvZm2-induced expression by at least 3-fold (Figure 3b). Comparing the exact levels of output
119 with and without EnvZm2, we found that EnvZt# variants are capable of overriding the initial phosphorylation state
120 of OmpR-VP64 to ultimately set a defined level of output (Supplementary Figure 5). Most strikingly, all EnvZm3t#
121 variants showed potent and nearly identical deactivation of OmpR-driven expression back to baseline levels
122 regardless of their rotational conformation (Figure 2c), indicating that all GCN4-fused truncations possess similar
123 phosphatase activities. These data suggest that the fusion protein itself takes on a conformation that is amenable to
124 phosphatase activity, possibly due to the formation of a more rigid structure¹⁸, whereas the rotational state of the DHP
125 domains mostly affects autophosphorylation.

126 To more quantitatively compare the activation and deactivation of OmpR-driven expression by each of the EnvZ

127 variants described above, we fit simple first-order models to estimate the dosages of each variant needed for
128 half-maximal activation or deactivation ($K_{1/2}$) of the output (Supplementary Figure 6). Notably, the EnvZm3t#
129 variants deactivated output expression with $K_{1/2}$ values 2- to 3-fold smaller than our previous best putative
130 phosphatase, EnvZm1[AAB], and 10- to 20-fold smaller than the enzymatically null variant EnvZm0m1m2m3
131 (Supplementary Figure 6), indicating potent phosphatase activity. Moving forward, we chose to use the variant
132 EnvZm3t10 as our phosphatase because it has one of the lowest values of $K_{1/2}$ among all EnvZ variants and
133 completely deactivates the output down to basal levels (Figure 3b & Supplementary Figure 6).

134 To ensure that the observed putative phosphatase activity is not explained by formation of partially or completely
135 inactive heterodimers between any putative phosphatases and EnvZm2, we repeated the experiments described above
136 with CpxA in place of EnvZm2 (Supplementary Figure 7a). CpxA has weak off-target kinase activity for OmpR²⁰,
137 and broadly, heterodimerization between different HKs is rare⁴¹. In the presence of CpxA, the putative phosphatases
138 similarly, and in some cases more potently, deactivate OmpR-driven expression (Supplementary Figure 7b-c). Thus,
139 the observed output deactivation is independent of how OmpR-VP64 is phosphorylated.

140 Direct cellular verification of EnvZm3t10 phosphatase activity is challenging due to the acid-lability of
141 phosphohistidine and phosphoaspartate bonds^{42,43} and lack of commercial antibodies against P-OmpR. To verify that
142 EnvZm3t10 acts as a phosphatase, we thus carried out additional control experiments. Deactivation of OmpR-driven
143 output by EnvZm3t10 is abolished when adding mutations predicted to eliminate its phosphatase activity, or using
144 constitutively active variants of OmpR-VP64 (Supplementary Figure 8). Thus, the observed putative phosphatase
145 activity is not caused by blocking interactions between the kinase and OmpR-VP64, nor by sequestration of
146 OmpR-VP64. It is thus unlikely that EnvZm3t10 is acting through a mechanism other than direct dephosphorylation
147 of P-OmpR-VP64.

148 **2.3 Tuning kinase-output responses via phosphatase activity**

149 We next constructed a family of tunable genetic devices in which the tunability arises from a CMC between our
150 preferred kinase (EnvZm2) and phosphatase (EnvZm3t10) acting on OmpR-VP64 (Figure 4a). The inputs to these
151 devices are the enzymatic activities of the kinase (u_K) or phosphatase (u_P), or factors that affect such rates. The
152 device outputs are the transcriptional and translational products driven by OmpR-VP64. To evaluate the tunability of
153 our engineered CMC, we compared the level of OmpR-VP64-driven output across combinations of kinase and
154 phosphatase levels, with the phosphatase level regulated at the DNA and protein levels (Figure 4b-c).

155 First, we titrated both kinase and phosphatase levels by dosing in different amounts of plasmid DNA per sample
156 using poly-transfection⁴⁴ (Figure 4b). The 2D input-output map indicates that output expression increases gradually
157 with the ratio of kinase to phosphatase dosages (Figure 4b, left). As the dosage of phosphatase increases, the amount
158 of kinase needed to activate the output increases (Figure 4b, center), indicating a decreased sensitivity to kinase input

159 levels. Likewise, as the level of kinase increases, the amount of phosphatase needed to deactivate the output also
160 increases (Figure 4b, right). Both results are in accordance with standard models of CMCs²³ (see Supplementary
161 Note 1 for our derivation).

162 Following the above results, we predicted that we could tune output expression through modulation of
163 phosphatase stability (Figure 4c). To do so, we fused the phosphatase to small molecule-inducible degradation
164 domains (DDs) DDd⁴⁵ and DDe⁴⁶, which are stabilized by addition of trimethoprim (TMP) and 4-hydroxytamoxifen
165 (4-OHT), respectively. N-terminal fusions of both DDd and DDe showed the highest fold-changes in output
166 expression upon addition of the cognate small molecule (Supplementary Figure 9); we chose to move forward with
167 DDd/TMP for further testing due to lower background signal than DDe/4-OHT. Titration of both the kinase dosage
168 and TMP concentration shows that the output is high only when the kinase is high and TMP is low (Figure 4c, left).
169 Addition of TMP decreases the sensitivity of the output to kinase (Figure 4c, center) and addition of kinase decreases
170 the sensitivity of the output to TMP (Figure 4c, right).

171 The response of the TMP-tuned design to kinase and TMP levels depends on the initial level of phosphatase in the
172 cell. If the level of phosphatase is initially too high, the degradation domain cannot suppress it enough to enable
173 output induction by the kinase; conversely, if the initial level of phosphatase is too low, the kinase dominates the
174 CMC even without any TMP added (Supplementary Figure 10). Thus, there is an optimal level of phosphatase where
175 TMP-induced deactivation of gene expression is maximized.

176 **2.4 Engineered, cell type-specific signaling responses**

177 In addition to ectopically-expressed factors, endogenous cellular factors can also be plugged in as inputs to the
178 kinase (u_K) and phosphatase (u_P) in our engineered CMC, enabling device performance to be tuned based on factors
179 such as the state of the cell. One particularly useful class of intracellular inputs are miRNAs, which are differentially
180 expressed across cell types⁴⁷ and can be used to identify specific cell states⁴⁸. Building on our CMC, we expected
181 that endogenous miRNAs can be targeted to the mRNAs of the kinase or phosphatase to decrease or increase output
182 expression, respectively (Figure 5a). An important and difficult challenge in miRNA sensing is to achieve good on/off
183 responses from the conversion of "high" miRNA inputs into high levels of output expression⁴⁴. We thus investigated
184 our CMC as a scaffold for improving miRNA input processing and generating cell-type specific signaling responses.

185 As a proof of concept, we built a sensor for a cancer-associated miRNA, miRNA-21-5p (miR-21), which has
186 previously been used to classify HeLa cells as distinct from HEK cells^{44,48}. To do so, we placed four miR-21 target
187 sites (T21) in both the 5' and 3' UTRs of the phosphatase transcription unit (Figure 5b). As a control, we replaced the
188 miR-21 target sites with four target sites for the synthetic miR-FF4 (TFF4)⁴⁹. In cells expressing miR-21, we
189 expected the phosphatase to be knocked down, thereby dramatically shifting the balance of the CMC to favor

190 phosphorylation of OmpR-VP64 and thus activation of the output. Since P-OmpR has only a ~10-30-fold higher
191 affinity for DNA binding compared to OmpR⁵⁰ (which we validated in HEK-293FT cells – Supplementary Figure
192 13), we included an endoribonuclease (endoRNase)-based incoherent feedforward loop (iFFL)⁵¹ to constrain
193 cell-to-cell variance in the expression level of OmpR-VP64 (Supplementary Figure 12). This is helpful due to the
194 high DNA dosage variance of transfections, within which only a small subset of cells typically receive the ideal
195 dosage of OmpR-VP64, and cells that receive high DNA dosages are susceptible to spurious activation of output
196 expression by unphosphorylated OmpR.

197 To test the circuit, we first considered the effect of miR-21 on the kinase-output dose-response curve. We expected
198 that endogenous expression of miR-21 would selectively sensitize output expression to kinase levels in HeLa cells.
199 Without the phosphatase, the kinase can induce output expression in both HEK and HeLa cells with either circuit
200 variant (T21 or TFF4), though with stronger output in HeLa cells (Figure 5c, left). When the phosphatase is present
201 and highly expressed, it suppresses output induction by the kinase in all cases except in HeLa cells with the T21
202 circuit variant (Figure 5c, right). Note that without the iFFL, the output expression has higher ‘leaky’ background
203 expression at low ratios of kinase to phosphatase dosages (Supplementary Figures 14 & 15). Depending on the
204 phosphatase dosage, the T21 variant in HeLa cells has between 10- to 1000-fold higher sensitivity to kinase input
205 than the TFF4 variant (Supplementary Figure 18). Thus, these results illustrate a novel application of miRNA sensors
206 for cell-type specific tuning of signaling responses.

207 To optimize our sensor for cell type classification, we followed the approach of Gam *et al.*⁴⁴ to systematically
208 compare the percent of cells positive for output expression at different ratios of each circuit component using
209 poly-transfection. In our previous classifier designs, a transcriptional repressor such as LacI⁴⁸ or BM3R1⁴⁴ is
210 repressed by the miRNA, thereby de-repressing output transcription. Poly-transfection analysis showed that miRNA
211 sensing in such systems is difficult to optimize, requiring the expression level of the repressor to be not too high to
212 prevent de-repression and not too low to prevent repression in the first place⁴⁴. In our current design, miRNA sensing
213 is instead optimized by the ratio of kinase to phosphatase activity, which is a more flexible and easily tuned quantity.

214 We found that a 1:1:0.5 ratio of Kinase:Phosphatase:Output plasmids (the latter of which was co-delivered with
215 the CasE/OmpR-VP64 iFFL) maximized classification accuracy for the T21 vs TFF4 variants in HeLa cells
216 (Supplementary Figure 16). At this ratio, we obtained a significant ~50% increase in cells positive for output reporter
217 between the circuit variants in HeLa cells and a ~55% increase between HeLa and HEK-293 for the T21 variant ($p =$
218 0.0017 and 0.0056 respectively, paired two-tailed Student’s T-test – Figure 5d). The area under the curve (AUC) of
219 the receiver operating characteristic (ROC) curve of the circuit was 0.83 ± 0.01 when comparing T21 vs TFF4
220 variants in HeLa cells and 0.93 ± 0.01 when comparing the T21 variant in HEK-293 vs HeLa cells (Supplementary
221 Figure 16). Examining various combinations of dosages of the kinase, phosphatase, and output reporter, we found
222 that the AUC of the resulting ROC-like curve of our phosphorylation-based classifier (0.93 ± 0.04 – Supplementary

223 Figure 17) is higher than that of our recently-optimized transcriptional repressor-based classifier (0.84 – see SI Fig.
224 16 in Gam *et al.*⁴⁴) for discriminating HEK vs HeLa cells, indicating improved overall performance for cell-type
225 classification. Thus, the CMC can be used for robust miRNA input processing with minimal tuning effort through
226 finding the optimal ratio of kinase to phosphatase activities.

227 **2.5 Design of a phosphorylation-based feedback controller**

228 The response of expressed genes to their extracellular (or intracellular) inputs are often stochastic and thus
229 imprecise across individual cells^{52,53}. In addition, the intracellular context affects the level of gene expression
230 induced by signaling^{29,30}, due to factors such as off-target interactions⁵⁴ or resource competition^{51,55,56} among
231 engineered genes. To remedy these issues and enable construction of signaling circuits that enforce precise and
232 robust signaling responses across cells, we applied feedback control to our CMC (Figure 6a). In both natural and
233 synthetic systems, feedback control can reduce cell-to-cell variance of gene expression in response to signal
234 inputs⁵⁷⁻⁵⁹. Negative feedback has also been used to make gene expression robust to perturbations that affect
235 processes within the feedback loop⁶⁰⁻⁶². An advantage of our controller design is that it can be applied without
236 modifying any promoters or intermediate RNA or protein species in the pathway (*e.g.* via the generation of fusions),
237 and simply requires a modification of the output mRNA.

238 In our controller, the phosphatase is co-expressed with the output gene via a 2A linker⁶³ and suppresses its own
239 production via dephosphorylation of P-OmpR-VP64 (Figure 6b). Feedback strength can be tuned through TMP
240 regulation of the DDD-fused phosphatase. The level of output set by the controller arises from competitive
241 phosphoregulation of OmpR-VP64 by the kinase and feedback phosphatase. In an ideal system operating with both
242 enzymes saturated, the concentrations of the phosphatase and the output species become insensitive to disturbances
243 affecting their gene expression processes (see Model Box). As TMP selectively regulates phosphatase but not output
244 stability, it can be used as an input to the controller to tune the strength of the feedback. Under the ideal conditions
245 presented above and as long as OmpR-VP64 has not saturated the output promoter, the relationship between the
246 levels of kinase and output is independent of both the exact mechanism by which OmpR-VP64 activates output
247 expression as well as of any perturbations in the transcription and translation processes of the output/phosphatase (see
248 Model Box).

249 To evaluate the performance of the feedback controller, we first measured the kinase-output responses for open
250 loop (OL) and closed loop (CL) variants. The OL system was made by replacing the phosphatase with Fluc2, which
251 has no effect on OmpR phosphorylation (Figure 2b-c). Since the presence of negative feedback reduces the level of
252 output expression for a given input level of kinase, we tested several OL variants in which the amount of output
253 reporter in transfections was reduced by 3x, 9x, 27x, or 81x (respectively referred to as Fluc2/3, Fluc2/9, Fluc2/27,

254 and Fluc2/81). We define kinase responsiveness as maximal output fold-change in the presence versus absence of
255 kinase. The kinase responsiveness of the OL systems varies from ~10- to ~55-fold. For the CL system variant
256 without DDD fused to the phosphatase, the kinase responsiveness is ~3.5-fold (Figure 6c, left – see Supplementary
257 Figures 19-22 for full poly-transfection scheme and data). Adding DDD to the phosphatase increases the CL kinase
258 responsiveness to ~7.6-fold without TMP, and 6.4-fold for the lowest non-zero amount of TMP that we tested: 0.001
259 μM (Figure 6c, right). The kinase responsiveness of the CL system decreases as more TMP is added (and thus the
260 phosphatase is stabilized) to the point of approximately matching that of the non-DDD CL system (Figure 6c, right).
261 The maximum output level of the DDD CL system is up to 10-fold higher than that of the non-DDD CL system and
262 within ~5-fold of that of the OL system. Thus, tuning the feedback strength via TMP allows the CL system to
263 recover approximately one third of the dynamic range of the OL system.

264 In the absence of kinase input, we see similar levels of noise in output expression for all OL and CL variants;
265 however, as the dosage of kinase is increased, we observe a decrease in noise for CL variants and an increase in noise
266 for OL variants (Figure 6d). At high dosages of kinase, the output noise for OL devices decreases again, but does not
267 reach the low noise achieved in CL devices. The higher noise in OL systems can be attributed to a more digital-like
268 transition in output expression per cell as the kinase dosage increases, whereas in CL systems we observe a smooth,
269 unimodal shift in output expression per cell (Figure 6e, see Supplementary Figure 23 for all variants). The decrease
270 in noise in CL expression as a function of increasing kinase can likely be attributed to the increasing concentration of
271 P-OmpR-VP64 on which the phosphatase can actuate negative feedback. Interestingly, tuning feedback strength with
272 TMP appears to have little effect on the magnitude of output noise observed (Supplementary Figure 24), suggesting
273 that the faster degradation of the phosphatase did not push our system into a regime where the negative feedback is
274 significantly attenuated.

275 Comparing the noise as a function of output level for all CL and OL variants, we can see that the noise in the OL
276 systems peaks at intermediate absolute levels of output (regardless of the kinase dosage needed to achieve such an
277 output level for a given OL variant), whereas the noise in the CL systems decreases as the output increases due to the
278 factors described above (Figure 6f). The pattern of noise in the OL variants can potentially be explained by stochastic
279 transcriptional variation among cells when the output promoter is not saturated. Through negative feedback, the CL
280 system is likely able to suppress this source of noise.

281 **2.6 Robustness to perturbations via feedback control**

282 According to our mathematical modeling comparing the OL and CL circuits, the presence of negative feedback is
283 expected to impart robustness to perturbations that affect expression of the output protein (see Model Box). We
284 analyzed robustness in terms of both fold-changes in gene expression resulting from the perturbations and a

285 robustness score (100% minus the percent deviation from the unperturbed level); a high degree of robustness is
286 indicated by small absolute fold-changes and high robustness scores. We tested the capability of the CL system to
287 impart robustness of output expression levels to perturbations that model off-target regulation and resource loading
288 (Figure 7a). To model off-target regulation by an endogenously- or ectopically-expressed gene regulator such as a
289 miRNA, we expressed miR-FF4, which binds and cleaves a target site (TFF4) placed in the 3' UTR of the
290 output/phosphatase mRNA, thereby causing mRNA degradation. To model resource loading, we expressed
291 Gal4-VPR, which strongly sequesters transcriptional resources, such as those recruited by the VP64 activation
292 domain fused to OmpR, thereby reducing transcription of other genes⁵¹. In addition to the modeled effects, these
293 perturbations are useful because they affect output production both before (Gal4-VPR) and after (miR-FF4)
294 transcription, enabling comparison of the CL system's ability to respond to perturbations at different stages of gene
295 expression.

296 As expected, we found that the CL system is indeed more robust to miR-FF4 and Gal4-VPR perturbations than
297 comparable OL variants (Figure 7b-e). Detailed comparisons of the response of all OL and CL variants to both
298 perturbations are provided in Supplementary Figures 25 & 26. For illustration, we highlight and compare two OL and
299 two CL variants with similar basal output levels in the absence of kinase (Fluc2, Fluc2/3, EnvZm3t10,
300 DDd-EnvZm3t10 + 0.001 μ M TMP – Figure 7b). Without kinase, there is little difference between the effects of
301 miR-FF4 and Gal4-VPR on the OL and CL systems (Figure 7c, left panels), consistent with the expected lack of
302 feedback actuation in the absence of P-OmpR-VP64 and our earlier findings of similar levels of noise in the same
303 regime (Figure 6d). At higher kinase input levels, the fold-changes in output expression for the CL variants in
304 response to both perturbations are substantially less than those of the OL variants (Figure 7c, right panels).

305 The relative decrease in fold-changes as a function of kinase input dosage is plotted in Figure 7d for two levels of
306 miR-FF4 and Gal4-VPR perturbations that knock down the OL systems to similar degrees. At medium-to-high
307 kinase input levels, the feedback controller can respond to the perturbations by sustaining the output level to within
308 2-4-fold of the nominal (unperturbed) levels, improving significantly over the 6-10-fold changes observed in the OL
309 systems. The relatively weaker output suppression by Gal4-VPR for both the OL and CL variants at low kinase
310 dosages may result from generally weaker effects of transcriptional resource sequestration on basal transcription vs
311 activated transcription⁶⁴. This may offset the general increased susceptibility of the CL system to perturbations in the
312 low-kinase regime, causing the CL systems to be more evenly perturbed by Gal4-VPR across kinase dosages.

313 Because negative feedback reduces output expression, and since both miR-FF4 and Gal4-VPR knock down gene
314 expression, a full comparison of the effects of these perturbations on the OL and CL systems must account for
315 differences in the nominal output expression level. This is because lower nominal output levels can have a reduced
316 measurable dynamic range of knockdown due to detection limits imposed by the autofluorescence background. To
317 account for varying nominal output levels for OL and CL systems at different kinase input levels, we compared the

318 nominal output level versus robustness score for each device. Collating all CL and OL variants at the same miR-FF4
319 and Gal4-VPR dosages as in Figure 7d, we can see that the CL systems are nearly always more robust than the OL
320 systems for a given nominal output level (Figure 7e). The only substantial overlap in the plots between the OL and
321 CL systems occurs at low kinase inputs to the CL system. Quantitatively, for a given nominal output level, we see a
322 20-30 percentage point increase in robustness score for the CL systems compared to the OL variants. Comparisons
323 across additional dosages of each perturbation show similar results (Supplementary Figures 27 & 28). Thus, our
324 phosphorylation-based feedback controller is capable of reducing the impact of perturbations on expression of the
325 output gene at both the transcriptional and post-transcriptional levels. Coupled with the reduction in noise (Figure 6),
326 these data indicate that the feedback controller can successfully impart precise, tunable, and robust control over gene
327 expression in mammalian cells.

328 **3 Model Box**

Here we develop a mathematical model to show that covalent modification cycle (CMC)-mediated feedback enables the expression level of a regulated gene to be robust to disturbances. In particular, for a fixed kinase level (K_t), we treat the genetic circuit shown in Figure 7 as feedback interconnection of two dynamical processes with input/output (I/O): an engineered CMC that takes phosphatase concentration (P_t) as input and outputs P-OmpR-VP64 concentration (X^*), and a gene expression process that takes X^* as input to produce the phosphatase P_t as output. We use a standard Goldbeter-Koshland model²³ for the dynamics of the CMC:

$$\frac{d}{dt}X^* = \theta_k \frac{(X_t - X^*)K_t}{(X_t - X^*) + K_{M,k}} - \theta_p \frac{X^*P_t}{X^* + K_{M,p}}, \quad (1)$$

where θ_k and θ_p are catalytic rate constants of the kinase and the phosphatase, respectively, $K_{M,k}$ and $K_{M,p}$ are their respective Michaelis-Menten constants, and X_t is the total amount of OmpR-VP64 (*i.e.*, OmpR-VP and P-OmpR-VP). The expression of P_t is regulated by an OmpR-activated promoter, which gives rise to the following dynamics:

$$\frac{d}{dt}P_t = \alpha(1 - w)\phi(X^*) - \gamma P_t, \quad (2)$$

where α is the production rate of P_t that lumps the rate constants for transcription, translation, and mRNA decay, $\phi(\cdot)$ is a Hill function satisfying $\phi' > 0$ for all X^* , γ is the protein decay rate constant, and $0 \leq w < 1$ is a disturbance that models the fold change in production rate of P_t , which could either arise from indirect transcriptional repression via resource loading or from direct post-transcriptional repression via miRNA (see Figure 7). The output from this feedback-regulated gene is $Y = \rho P_t$, since the output protein and phosphatase are co-transcribed but produced as separate proteins using a 2A-linker. We find that the relative sensitivity of output to disturbance w for this closed-loop

system (1)-(2) at a given output level Y is

$$\mathcal{S}_{\text{CL}}(Y) = \frac{1}{Y} \cdot \left| \frac{dY}{dw} \right| = \frac{1}{1-w} \left[1 + \frac{\alpha}{\gamma}(1-w) \left| \frac{d}{dY}(\phi \circ h) \right| \right]^{-1}, \quad (3)$$

where h is the transfer curve of the CMC. In comparison, when the CMC in (1) is not connected with (2), the relative sensitivity of y to disturbance w for the open-loop system (2) is $\mathcal{S}_{\text{OL}} = \frac{1}{1-w}$. Hence, we have $\mathcal{S}_{\text{CL}} < \mathcal{S}_{\text{OL}}$ for all y regardless of where the sensitivity is evaluated. This implies that the closed-loop system is always more robust than the open-loop system to disturbance w . To enable near-perfect adaptation to w , it is sufficient to increase $T := \left| \frac{d}{dY}(\phi \circ h) \right| = |h' \cdot \phi'|$. In particular, if $T \rightarrow \infty$, then $\mathcal{S}_{\text{CL}} \rightarrow 0$, implying that the closed-loop system can perfectly adapt to w . Specifically, for any fixed X^* and y , there exists sufficiently small $K_{M,p}$ and sufficiently large X_t to make $|h'|$ arbitrarily large. On the other hand, to ensure T is large, $|\phi'|$ must not be too small. This requires us to design the system so that the OmpR-activated promoter is not saturated. Hence, the K_D of binding between phosphorylated OmpR and its target promoter must not be too small²⁷. Promoter saturation limits the ability of the output to respond to changes in OmpR phosphorylation, and thus can limit the benefit of the negative feedback to achieve robustness to perturbations. Under the ideal operating conditions described above, both enzymes are saturated by their substrates, which is possible for a small $K_{M,p}$ and large X_t . Specifically, if $K_{M,p} \ll X^*$ and $X_t \gg K_{M,k}$, equation (1) can be approximated by $dX^*/dt = \theta_k K_t - \theta_p Y/\rho$, leading to quasi-integral feedback control²⁷.

4 Discussion

Here, we developed tunable and precise signaling circuits in mammalian cells that are robust to perturbations using engineered CMCs derived from bacterial two-component signaling (TCS) proteins (Figure 1). We first screened engineered variants of the *E. coli* histidine kinase (HK) EnvZ to isolate kinase and phosphatase activity from this bifunctional protein (Figures 2 & 3). We demonstrated tunability in kinase-induced gene expression responses conferred by small molecule-inducible expression of a phosphatase (Figure 4). Building upon this tunability, we showed that incorporating target sites for endogenous miRNAs can be used to create cell type-specific signaling responses through knockdown of phosphatase expression. Co-expressing the phosphatase with the output, we created a tunable negative feedback loop that reduces both cell-to-cell variation and sensitivity to perturbations of kinase-induced gene expression (Figure 6 & 7).

Combined with recent advances in utilizing TCS proteins to engineer synthetic receptors in mammalian cells^{12,13} and to rewire the specificity of response regulators (RRs) in bacteria⁶⁵, our platform will enable construction of sophisticated synthetic signaling systems that can connect intracellular and extracellular inputs to diverse target output in mammalian cells. While much work has so far focused on synthetic receptor engineering¹⁰, incorporation of downstream signal processing moieties to improve signaling pathway function has only recently begun to be

357 explored⁶⁶. In particular, the ability to easily tune signaling pathway activity through phosphatase expression and the
358 ability to robustly control downstream gene expression processes will facilitate the creation of synthetic signaling
359 systems that can operate across diverse cellular contexts. In the future, our circuits can form the basis for advanced
360 cellular computing⁶⁷ and feedback control⁶⁸ architectures. In addition, the phosphorylation cycles in our CMC-based
361 systems may serve to effectively buffer the effects of retroactivity⁶⁹ from downstream target sites loading the
362 phospho-TF, provided that the phosphorylation reactions are sufficiently fast and the enzyme concentrations are
363 sufficiently high⁷⁰. Utilizing TCS components comprising multiple His-Asp phosphorelays¹⁸ may further buffer the
364 effects of retroactivity^{70,71}. Finally, connecting signaling pathway activity to endogenous gene regulation, such as
365 through miRNA regulation of pathway components, will facilitate applications in guiding differentiation or
366 programming custom signaling for different cellular states.

367 The high degree of orthogonality among existing TCS pathways⁷²⁻⁷⁴ and the relative ease of finding new
368 orthogonal HK/RR pairs⁷⁵ indicates that TCS pathways will be a bountiful source of orthogonal signaling pathways
369 for use in mammalian cells. To support this effort, we identified several HK-RR pairs that show good orthogonality in
370 mammalian cells (Supplementary Figures 29-31). Though TCS pathways are absent in animals¹⁴, histidine and
371 aspartate phosphorylation is more prevalent than previously thought⁴³. The lack of observed histidine to aspartate
372 phosphotransfer in animals indicates a strong likelihood of orthogonality between TCS pathways and existing
373 signaling networks in animal cells, though future work will be needed to examine possible cross-talk.

374 Through the implementation of feedback control via CMCs, we have opened the door to creating increasingly
375 precise and robust responses in engineered signaling pathways. Reducing cell-to-cell variation in signaling output
376 can be critical for ensuring that cells in a population make uniform, rather than multi-modal or stochastic, decisions.
377 Reducing sensitivity of output expression to perturbations will help further control individual cellular
378 decision-making and ensure that engineered signaling systems can operate across diverse cell types and states⁵¹. In
379 the future, it may be possible to improve the robustness to perturbations conferred by our feedback controller. To
380 achieve near-perfect adaptation to perturbations, the system parameters need to be tuned such that it can operate as a
381 quasi-integral feedback controller^{27,76}. We identified that the K_M of the phosphatase is likely similar to or higher than
382 the K_D of P-OmpR, reducing the efficacy of the feedback (see Model Box). Increasing $\frac{K_D}{K_M}$ helps ensure that the
383 phosphatase is saturated with P-OmpR while the output promoter is not, both of which are critical conditions for the
384 feedback to work in a quasi-integral manner²⁷ (see Model Box). Further discussion of possible future approaches to
385 achieve quasi-integral feedback control with our system are discussed in Supplementary Note 2.

386 In addition to set point regulation, negative feedback may also speed up the dynamics of a regulated system, as has
387 been observed previously using transcriptional negative feedback⁷⁷. However, faster dynamics of the regulated
388 system depends on controller architecture and parameters. In particular, while controllers incorporating integral
389 action are known to improve steady state regulation performance, they may not speed up dynamics⁷⁸, which is why

390 integral control is usually combined with proportional and derivative control in engineering⁷⁹. In terms of analyzing
391 the dynamics of our system, it is important to consider that it was tested with transient transfections, which places
392 limits on measurement fidelity as well as operational responses. DNA dilution during transient transfection prevents
393 the system from achieving a nonzero steady-state, and also causes the set point to change over time as the kinase level
394 increases then decreases. Further, DNA dilution causes controller performance to degrade as the expression of OmpR
395 decays and the enzymes begin to operate outside the saturation regime needed for integral control (see Model Box).
396 Thus, to precisely evaluate the dynamic response of our controllers and any modified variants thereof, future studies
397 will benefit from genomic integration of the circuits.

398 In natural systems, feedback control plays a critical role in regulating signaling pathway activities. Both negative
399 and positive feedback are common in TCS pathways⁸⁰. As with the robustness to perturbations conferred by our
400 feedback controller, negative feedback in natural and engineered TCS pathways in bacteria also allows for adaptation
401 to signal inputs^{25,72,80,81}. A conceptually similar controller to our design is found in bacterial chemotaxis, in which
402 feedback control via reversible methylation of the receptor protein Tar enables near-perfect adaptation of flagellar
403 motion to chemoattractants^{76,82}. Another close analog can be found in the human ERK1/2 MAPK (mitogen-activated
404 protein kinase) pathway⁸³. In this pathway, Mek is analogous to our HK kinase, Erk is analogous to OmpR-VP64
405 (though Erk itself only indirectly activates transcription through its targets^{84,85}), and the Erk-induced phosphatases
406 DUSP5/6 are analogous to our HK phosphatase^{83,86}. It has been observed that the expression levels of DUSP5/6 are
407 unaffected by ERK1/2 knockdown⁸⁷, which we propose may result from adaptation of DUSP5/6 levels to ERK1/2
408 levels due to the negative feedback loop. Negative feedback in both natural and engineered systems, including the
409 ERK1/2 MAPK pathway, has been shown to convert digital, multimodal input-output responses to more graded,
410 linear, and uniform responses^{57,58,88}. Likewise, our feedback controller is capable of imparting graded, uniform
411 activation of gene expression in the cell population. Overall, these examples highlight how feedback control plays an
412 important role in the functions of natural systems and will thus serve as a key building block for future synthetic
413 signaling pathways.

414 In addition to feedback control, natural signaling pathways also incorporate constitutive phosphatase and
415 regulators thereof to tune signaling functions across diverse cell types. For example, signaling through the T cell
416 receptor (TCR) is regulated by several inhibitory receptors such as CD45 and phosphatases such as PTPN22, which
417 suppress TCR pathway activation unless sufficiently high stimulus is encountered⁸⁹. In developing thymocytes,
418 miR-181a-5p suppresses expression of PTPN22, thereby allowing for TCR pathway stimulation at lower antigen
419 affinities, providing critical signals for survival and development towards mature T cells^{90,91}. In mature T cells, a
420 variety of miRNAs regulate TCR signaling, other signaling pathways, the cell cycle, and secretion, thereby tuning the
421 immunological responses of T cells to their environments⁹². Thus, tunable phosphatases and miRNA-regulated
422 signaling responses similar to the ones we developed can be powerful tools for achieving stage-specific control of

423 differentiation and tuning cell behavior in different contexts. Future designs may also incorporate miRNAs that
424 regulate kinase expression to provide an additional layer of tunability, for example by miRNAs that are lower in cell
425 types or states where higher signaling strengths are desired.

426 As synthetic biology progresses, the development of artificial signaling pathways that reflect natural pathways
427 through incorporation of multiples layers of negative feedback and tuning will facilitate increasingly sophisticated
428 and robust control of cellular behavior. The customizable signaling responses enabled through platforms such as ours
429 may be combined with engineered receptors^{12,13} and modular effectors⁶⁵ to engineer signaling pathways that
430 transmute extracellular inputs to various intracellular functions in mammalian cells. Such engineered signaling
431 pathways will enable precise cell-cell communication and environmental sensing, with applications in engineering
432 cell therapies, scaling up bioproduction, and programming development of stem cells into specific cells, tissues, and
433 organoids.

434 5 Methods

435 **Modular plasmid cloning scheme**

436 Plasmids were constructed using a modular Golden Gate strategy similar to previous work in our lab^{44,93}. Briefly,
437 basic parts ("Level 0s" [pL0s] – insulators, promoters, 5'UTRs, coding sequences, 3'UTRs, and terminators) were
438 created via standard cloning techniques. Typically, pL0s were generated via PCR (Q5 and OneTaq hot-start
439 polymerases, New England BioLabs (NEB)) followed by In-Fusion (Takara Bio) or direct synthesis of shorter inserts
440 followed by ligation into pL0 backbones. Oligonucleotides were synthesized by Integrated DNA Technologies (IDT)
441 or SGI-DNA. pL0s were assembled into transcription units (TUs – "Level 1s" [pL1s]) using BsaI Golden Gate
442 reactions (10-50 cycles between 16degC and 37degC, T4 DNA ligase). TUs were assembled into multi-TU plasmids
443 ("Level 2s" [pL2s]) using SapI Golden Gate reactions. All restriction enzymes and T4 ligase were obtained from
444 NEB. Plasmids were transformed into Stellar *E. coli* competent cells (Takara Bio). Transformed Stellar cells were
445 plated on LB agar (VWR) and propagated in TB media (Sigma-Aldrich). Carbenicillin (100 $\mu\text{g}/\text{mL}$), kanamycin (50
446 $\mu\text{g}/\text{mL}$), and/or spectinomycin (100 $\mu\text{g}/\text{mL}$) were added to the plates or media in accordance with the resistance
447 gene(s) on each plasmid. All plasmids were extracted from cells with QIAprep Spin Miniprep and QIAGEN Plasmid
448 Plus Midiprep Kits. Plasmid sequences were verified by Sanger sequencing at Quintara Biosciences. Genbank files
449 for each plasmid and vector backbone used in this study are provided in Supplementary Data. Plasmid sequences
450 were created and annotated using Geneious (Biomatters).

451 In addition to the above, we devised a new scheme for engineering synthetic promoters using what we call "Level
452 Sub-0" (pSub0) plasmids. The approach for creating promoters from pSub0 vectors is illustrated in Figure 32. In this
453 system, promoters are divided into up to 10 pSub0 fragments. Because the core elements of a promoter are typically

454 at the 3' end, we made the pSub0 position vectors start with the 3'-most element and move towards the 5' of the
455 promoter. Promoter position 1 (pP1) contains the transcription start site (TSS), the +1 position for transcription
456 initiation, and surrounding sequences. pP1 can also optionally contain transcriptional repressor binding sites (not
457 done in this study). pP2 contains the TATA box and other upstream core promoter elements⁹⁴⁻⁹⁶ as desired. Many of
458 the pP1 and pP2 sequences were derived from the minimal promoters studied by Ede *et al.*⁹⁷. Because the spacing
459 between the TATA box and +1 site are critical⁹⁸, we broke apart each minimal promoter at equivalent positions such
460 that they can be interchanged. pP1 and pP2 parts were generally created via PCR reactions using the base pSub0
461 backbone as a template and adding the inserts via primer overhangs and In-Fusion cloning. Positions 3-10 (pP3-10)
462 are 'enhancer' positions, wherein we generally encode binding sites (*i.e.* response elements) for transcriptional
463 activators (such as the RRs in this study), or enhancers from constitutive promoters (not done in this study). pP3-10
464 plasmids were made by directly ligating annealed primers into pSub0 pP3-10 backbones or through PCR followed by
465 In-Fusion. The annealed primers were synthesized with 4 bp offsets at each end to naturally create overhangs when
466 annealed. All pSub0 plasmids include BsaI binding sites in an analogous position to pL0s, such that pSub0s can be
467 used directly in place of pL0s when generating pL1s (the overhangs are compatible for up to four pSub0 inserts, see
468 Supplementary Table 1). Because pSub0s and pL0s use BsaI for cloning in the same way, insertion into pL0
469 backbones using BsaI Golden Gate is inefficient. To more efficiently clone pSub0s into pL0 P.2 (level 0 promoter)
470 plasmids, we thus generally first performed a Golden Gate reaction with the pSub0s separately from the pL0
471 backbone, then ligated the Golden Gate product with a pre-fragmented and gel-extracted pL0 backbone.

472 **Cell culture**

473 HEK-293 cells (ATCC), HEK-293FT cells (Thermo Fisher), and HeLa cells (ATCC) were maintained in
474 Dulbecco's modified Eagle media (DMEM) containing 4.5 g/L glucose, L-glutamine, and sodium pyruvate (Corning)
475 supplemented with 10% fetal bovine serum (FBS, from VWR). All cell lines used in the study were grown in a
476 humidified incubator at 37deg and 5% CO₂. All cell lines tested negative for mycoplasma.

477 **Transfections**

478 Cells were cultured to 90% confluency on the day of transfection, trypsinized, and added to new plates
479 simultaneously with the addition of plasmid-transfection reagent mixtures (reverse transfection). Transfections were
480 performed in 384-, 96-, 24-, or 6-well pre-treated tissue culture plates (Costar). Following are the volumes, number
481 of cells, and concentrations of reagents used for 96-well transfections; for 384-, 24- and 6-well transfections, all
482 values were scaled by a factor of 0.2, 5, or 30, respectively. 120 ng total DNA was diluted into 10 μ L Opti-MEM
483 (Gibco) and lightly vortexed. For poly-transfection experiments, the DNA dosage was subdivided equally among
484 each complex (*e.g.* for two complexes, we delivered 60 ng DNA in each, 40 ng for three complexes, *etc.*) The
485 transfection reagent was then added and samples were lightly vortexed again. The DNA-reagent mixtures were
486 incubated for 10-30 minutes while cells were trypsinized and counted. After depositing the transfection mixtures into

487 appropriate wells, 40,000 HEK-293, 40,000 HEK-293FT, or 10,000 HeLa cells suspended in 100 μ L media were
488 added. The reagent used in each experiment along with plasmid quantities per sample and other experimental details
489 are provided in Supplementary Data. Lipofectamine 3000 was used at a ratio of 2 μ L P3000 and 2 μ L Lipo 300 per 1
490 μ g DNA. PEI MAX (Polysciences VWR) was used at a ratio of 3 μ L PEI per 1 μ g DNA. FuGENE6 (Promega) was
491 used at a ratio of 3 μ L FuGENE6 per 1 μ g DNA. Viafect (Promega) was used at a ratio of 3 μ L Viafect per 1 μ g DNA.
492 The media of the transfected cells was not replaced between transfection and data collection. For all transfections
493 with TMP (Sigma-Aldrich) or 4-OHT (Sigma-Aldrich), the small molecules were added concurrently with
494 transfection complexes. In each transfection reagent-DNA complex, we included a hEF1a-driven transfection marker
495 to indicate the dosage of DNA delivered to each cell.

496 **Luciferase assays and analysis**

497 To measure RR-driven luminescence output in Supplementary Figure 29, we used the Promega Nano-Glo
498 Dual-Luciferase Reporter Assay System, following the manufacturer's instructions. Briefly, 6,000 HEK-293FT cells
499 were transfected using the FuGENE6 reagent with 25 ng total DNA comprising the plasmids hPGK:Fluc2
500 (pGL4.53), an hEF1a-driven HK, an hEF1a-driven RR, an RR-driven promoter expressing NanoLuc, and filler DNA
501 at 5 ng each. The cells were cultured in 20 μ L DMEM supplemented with 10% FBS in 384-well plates with solid
502 white walls and bottoms (Thermo Fisher) to facilitate luminescence measurements. 48 hours post-transfection, cells
503 were removed from the incubator and allowed to cool to room temperature. 20 μ L of ONE-Glo EX Reagent was
504 added directly to the cultures, and cells were incubated for 3 minutes on an orbital shaker at 900 revolutions per
505 minute (RPM). Fluc2 signal was measured on a BioTek Synergy H1 hybrid reader, with an integration time of 1 s. 20
506 μ L of NanoDLR Stop & Glo Reagent was then added, and cells were again incubated for 3 minutes on an orbital
507 shaker at 900 RPM. After waiting an additional 10 minutes following shaking, NanoLuc signal was measured on the
508 same BioTek plate reader, with an integration time of 1 s. NanoLuc signals were normalized by dividing by the Fluc2
509 signals, thereby accounting for differences in transfection efficiency among wells.

510 **Identification of optimal orthogonal TCS pairs**

511 To identify the optimal set of orthogonal TCS interactions, we ran a MATLAB script to score all possible
512 combinations of 4-7 HK-RR protein pairs. The script uses a scoring function to evaluate each particular subset of
513 HKs and RRs. The data input into the scoring function is a matrix of output expression levels driven by the RRs in
514 the presence of the selected HKs. The scoring function first identifies a reference value for each row and column by
515 iteratively finding the maximum value in the matrix, blocking off the rest of the values in its row and column, then
516 repeating until each row and column has one reference value. The reference value is then divided by the rest of the
517 values in its row and column, and the quotients are multiplied together to give a score. The scores for each reference
518 value are then again multiplied together to get a final score for a particular combination of HKs and RRs. After
519 iterating through all possible such combinations, the highest final score for a given submatrix size is selected. The

520 method gave qualitatively orthogonal combinations for up to 7 TCS pairs; we thus present the optimized 7-matrix in
521 Supplementary Figure 29.

522 **Flow cytometry**

523 To prepare samples in 96-well plates for flow cytometry, the following procedure was followed: media was
524 aspirated, 50 μ L PBS (Corning) was added to wash the cells and remove FBS, the PBS was aspirated, and 40 μ L
525 Trypsin-EDTA (Corning) was added. The cells were incubated for 5-10 minutes at 37deg C to allow for detachment
526 and separation. Following incubation, 80 μ L of DMEM without phenol red (Gibco) with 10% FBS was added to
527 inactivate the trypsin. Cells were thoroughly mixed to separate and suspend individual cells. The plate(s) were then
528 spun down at $400 \times g$ for 4 minutes, and the leftover media was aspirated. Cells were resuspended in 170 μ L flow
529 buffer (PBS supplemented with 1% BSA (Thermo Fisher), 5 mM EDTA (VWR), and 0.1% sodium azide
530 (Sigma-Aldrich) to prevent clumping). For prepping plates of cells with larger surface areas, all volumes were scaled
531 up in proportion to surface area and samples were transferred to 5 mL polystyrene FACS tubes (Falcon) after
532 trypsinization. For standard co-transfections, 10,000-50,000 cells were collected per sample. For the
533 poly-transfection experiment and transfections into cells harboring an existing lentiviral integration, 100,000-200,000
534 cells were collected per sample.

535 For all experiments, samples were collected on a BD LSR Fortessa equipped with a 405nm laser with 450/50nm
536 filter ('Pacific Blue') for measuring TagBFP or EBFP2, 488 laser with 530/30 filter ('FITC') for measuring EYFP or
537 mNeonGreen, 561nm laser with 582/15nm filter ('PE') or 610/20nm filter ('PE-Texas Red') for measuring mKate2 or
538 mKO2, and 640 laser with 780/60nm filter ('APC-Cy7') for measuring iRFP720. 500-2000 events/s were collected
539 either in tubes via the collection port or in 96-well plates via the high-throughput sampler (HTS). All events were
540 recorded and compensation was not applied until processing the data (see below).

541 **Flow cytometry data analysis**

542 Analysis of flow cytometry data was performed using our MATLAB-based flow cytometry analysis pipeline
543 (https://github.com/Weiss-Lab/MATLAB_Flow_Analysis). Basic processing steps with example data are
544 shown in Supplementary Figure 33 and follow the procedures described previously⁵¹. In addition, we frequently
545 utilized our new poly-transfection technique and associated methods⁴⁴ to characterize and optimize circuits.
546 Poly-transfection enables rapid and accurate assessment of dose-response curves for genetic components⁴⁴, such as
547 the kinases and phosphatases in our circuits. Full schematics describing each poly-transfection experiment are shown
548 in the SI (*e.g.* Supplementary Figure 2a).

549 Multi-dimensional binning of poly-transfection data was performed by first defining bin edges in each dimension
550 (*i.e.* for the transfection markers for each poly-transfection complex), then assigning each cell to a bin where the
551 cell's expression of these markers was less-than-or-equal-to the high bin edges and greater-than the low bin edges.
552 Bins with three or fewer cells were ignored (values set to NaN in the MATLAB code) to avoid skewing by outliers in

553 sparsely-populated samples (*e.g.* HeLa cells). Such binning is demonstrated via colorization of cells by their bin
554 assignment in the SI (*e.g.* Supplementary Figure 2b). In order to avoid the artefact of negative fold-changes,
555 non-positive fluorescence values were discarded prior to making measurements on binned or gated populations. In
556 the second and third experimental repeats of the miRNA-dependent signaling/classifier data in Figure 5 and
557 Supplementary Figures 14-18, a newly-prepared Output Marker plasmid was later discovered to have ~8-fold lower
558 concentration than expected due to a measurement error on the nanodrop. To account for this, the bins for the Output
559 Marker in those samples are shifted down by 10x (so as to match the same bin boundaries as in the first repeat).

560 To find the optimal ratio of components in the miR-21 sensor for high cell classification accuracy, we scanned
561 ratios between 1000:1 to 1:1000 of K:P and output plasmid:K/P, roughly halving the ratio between steps. At each
562 combination of ratios, a trajectory was computed and all cells within 0.25 biexponential units of the trajectory based
563 on euclidean distance were recorded. Accuracy was computed as described below, and accuracy values were
564 compared across all ratios for each experimental repeat. From this scanning of trajectories at different ratios of
565 components, we found that a 1:1:0.5 ratio of K:P:Output plasmid gave the highest accuracy. This optimal trajectory
566 was used to sub-sample cells for display in Figure 5f & Supplementary Figure 16, finding percent positive for output
567 in Figure 5g and calculating ROCs/AUCs in Supplementary Figure 16.

568 In the case of simple co-transfections and sub-sampled trajectories, cells were considered to be transfected if they
569 were positive for the output/transfection marker *or* the output reporter. When computing summary statistics from
570 binned data, such thresholding is unnecessary since binning already isolates the cell sub-population for measurement.

571 **Calculation of cell classification metrics**

572 Sensitivity was defined as the percent of cells positive for the output reporter in HeLa cells transfected with the
573 T21 circuit variant. Specificity was defined as 100 minus the percent of cells positive for the output in HeLa cells
574 with the TFF4 variant or in HEK-293 cells with the T21 variant. The former was considered the more ideal
575 comparison for evaluating classification performance due to higher overall expression of the circuit in HeLa cells
576 compared to HEKs (Supplementary Figure 14). Accuracy was computed by averaging sensitivity and specificity.

577 ROC curves in Supplementary Figure 16 were generated by scanning thresholds starting at -10^8 , then 0, then 15
578 log-spaced steps between 10^3 and 10^8 . The AUCs were computed individually for each experimental repeat by
579 trapezoidal area approximation using the MATLAB function 'trapz()'
580 (<https://www.mathworks.com/help/matlab/ref/trapz.html>). The AUC-like curves in Supplementary
581 Figure 17 were computed by fitting data from each experimental repeat with a bi-normal classification model in
582 MATLAB (see below for details of the fitting algorithm used).

583 **Calculation of p-values**

584 P-values shown in Figure 5 were computed using the MATLAB function 'ttest()'
585 (<https://www.mathworks.com/help/stats/ttest.html>). Samples were paired per experimental repeat and

586 the test was two-tailed.

587 **Calculation of fold-changes and robustness scores**

For quantifying the effects of EnvZ variants and perturbations, we measured fold-changes by dividing the median output level of each sample by that of the equivalent sample in the absence of the EnvZ variant or perturbation. For perturbation experiments, the level of output absent perturbation is referred to as the nominal output level.

$$\text{Fold-}\Delta(\text{Input/perturbation bin}_x) = \frac{\text{Output}(\text{Input/perturbation bin}_x)}{\text{Output}(\text{Input/perturbation bin}_1)} \quad (4a)$$

588 Where \log_2 -transformed fold-changes are shown for experiments with multiple repeats, the values shown are the
589 mean of the \log_2 -transformed fold-changes, rather than the \log_2 -transformation of the mean of the fold-changes. This
590 order of operations ensures that standard deviations of the fold-changes can be computed directly on the
591 \log_2 -transformed scale.

We computed robustness scores from the fold-changes using the formulae below:

$$\text{Robustness}(\text{Perturbation bin}_x) = 100 \cdot \left(1 - \left|1 - \text{Fold-}\Delta(\text{Perturbation bin}_x)\right|\right) \quad (5a)$$

592 **Quantification of cell-to-cell output variance**

593 To measure noise, we computed the interquartile range (IQR) of the output distributions. As we chose the median
594 to represent the middle of the distribution, the IQR is a corresponding non-parametric measurement of noise. Since
595 gene expression noise is approximately log-distributed, we \log_{10} -transformed the data prior to computing the IQR.
596 As with calculations of the medians, negative fluorescent values were discarded when computing the IQR to avoid
597 artefacts.

598 **Model fitting**

599 Where possible, fluorescent reporters were used to estimate the concentration of a molecular species for the
600 purpose of model fitting.

601 For fitting all models, we used the MATLAB function 'lsqcurvefit()' (https://www.mathworks.com/help/optim/ug/lsqcurvefit.html), which minimizes the sum of the squares
602 of the residuals between the model and the data. In general, fits were made with cells subsampled from bins, as
603 indicated for each figure. In Supplementary Figure 17, the fits were made using the true/false positive rates for each
604 bin. Fits were always performed individually per experimental repeat, then means and standard deviations were
605 computed for individual fit parameters.

606 Goodness of fit was measured by computing the normalized root-mean-square error CV(RMSE) using the
607 following formula:
608

$$\text{CV(RMSE)} = \frac{\sqrt{\frac{1}{\bar{y}} \sum_i (y(x_i) - f(x_i))^2}}{\bar{y}}$$

609 Where $y(x_i)$ is the value of the data at the input value x_i , \bar{y} is the mean of y for all values of x , and $f(x_i)$ is the
610 function output at input value x_i .

611 Fitting functions:

612 Activation of transcription by OmpR-VP64:

$$y = \alpha_0 + (\alpha - \alpha_0) \frac{x^2}{K_{1/2}^2 + x^2} \quad (6)$$

613 The cooperativity of OmpR was assumed to be two because it forms a dimer once phosphorylated to bind
614 DNA^{15,99}.

615 Activation of OmpR-VP64-driven expression by kinase: (see Supplementary Note 1 for more details):

$$y = \alpha_0 + (\alpha - \alpha_0) \frac{x^2}{K_{1/2}^2 + x^2} \quad (7)$$

616 Deactivation of OmpR-VP64 by phosphatase:

$$y = \alpha_0 + (\alpha - \alpha_0) \frac{K_{1/2}^2}{K_{1/2}^2 + x^2} \quad (8)$$

617 While OmpR-VP64 has not been completely tuned over to P-OmpR-VP64, the amount of P-OmpR-VP64 is
618 assumed to be proportional to the level of kinase because the production rate is only dependent on the kinase. In the
619 presence of the phosphatase, the decay rate becomes overwritten by the dephosphorylation reaction. Thus, these
620 proteins can be plugged directly into the OmpR-VP64 activation function, such that the kinase is proportional to
621 OmpR and the phosphatase is inversely so. Because of the inversion, the phosphatase function becomes a
622 repression-form Hill function.

623 The bi-normal fitting function for ROC curves is included with our MATLAB flow cytometry analysis package on
624 GitHub ('model_ROC.mat'). In short, the measurement of the fraction of cells positive for the output reporter is
625 assumed to follow a normal distribution with $\mu_1 = 0$ and $\sigma_1 = 1$ for the negative observations (TFF4 or HEK cells in
626 our case) and a normal distribution with unknown μ_2 and σ_2 for the positive observations (T21 in HeLa cells). μ_2 and
627 σ_2 are fit such that the true positive rate for a given false positive rate approximates that of the data.

628 **6 Data Availability**

629 Sequences for all plasmids used in this study are provided as GenBank files in Supplementary Data. New plasmids
630 used in this study will be available on Addgene upon publication. Raw .fcs files are available from the corresponding
631 authors upon reasonable request.

632 **7 Code Availability**

633 General MATLAB code for use in .fcs file processing and analysis are available under an open-source license in
634 our GitHub repository at https://github.com/Weiss-Lab/MATLAB_Flow_Analysis. Specific .m scripts for
635 each experiment are available from the corresponding authors upon reasonable request.

636 **8 Acknowledgements**

637 We would like to acknowledge Douglas Lauffenburger, Ahmad Khalil, and Conor McClune for helpful discussion.
638 Thanks to Bre DiAndreth for the MATLAB code to find optimal orthogonal TCS pairs; Jeremy Gam for the
639 MATLAB code to fit ROC curves and plasmids; both Jin Huh and Kalon Overholt for plasmids and helpful
640 discussion; and Nika Shakiba, Melody Wu, and Margaret Zhang for help with cloning pSub0 plasmids.

641 **9 Author Contributions**

642 R.D.J., Y.Q., D.D.V., and R.W. designed the study; R.W., D.D.V., and M.T.L. secured funding; R.D.J., K.I., and
643 B.W. performed the experiments; R.D.J. and B.W. analyzed the data; Y.Q. and R.D.J. developed the mathematical
644 models; R.D.J., Y.Q., D.D.V., and R.W. wrote the manuscript; R.D.J., Y.Q., K.I., B.W., M.T.L., D.D.V., and R.W.
645 edited and/or reviewed the manuscript.

646 **10 Funding**

647 This work was supported by the National Science Foundation (MCB-1840257).

648 **11 Competing Interests Statement**

649 The Massachusetts Institute of Technology has filed a patent application on behalf the inventors (R.D.J., J.H., and
650 R.W.) of phosphorylation-based miRNA sensor design described (US Provisional Application No. 16/528,772) and a
651 provisional application on behalf of the inventors (R.D.J., Y.Q., D.D.V., and R.W.) of the phosphorylation-based
652 feedback controller design described. The remaining authors declare no conflict of interest.

References

1. Jordan, J. D., Landau, E. M. & Iyengar, R. Signaling networks: The origins of cellular multitasking. *Cell* **103**, 193–200 (2000).
2. Lipsitz, Y. Y., Timmins, N. E. & Zandstra, P. W. Quality cell therapy manufacturing by design. *Nature Biotechnology* **34**, 393–400 (2016).
3. Brenner, M. J., Cho, J. H., Wong, N. M. & Wong, W. W. Synthetic Biology: Immunotherapy by Design. *Annual Review of Biomedical Engineering* **20**, 95–118 (2018).
4. Kamm, R. D. *et al.* Perspective: The promise of multi-cellular engineered living systems. *APL Bioengineering* **2**, 040901 (2018).
5. Rossi, G., Manfrin, A. & Lutolf, M. P. Progress and potential in organoid research. *Nature Reviews Genetics* **19**, 671–687 (2018).
6. Tewary, M., Shakiba, N. & Zandstra, P. W. Stem cell bioengineering: building from stem cell biology. *Nature Reviews Genetics* **19**, 595–614 (2018).
7. Kitada, T., DiAndreth, B., Teague, B. & Weiss, R. Programming gene and engineered-cell therapies with synthetic biology. *Science* **359**, eaad1067 (Feb. 2018).
8. Scheller, L. & Fussenegger, M. From synthetic biology to human therapy: engineered mammalian cells. *Current Opinion in Biotechnology* **58**, 108–116 (2019).
9. Johnson, M. B., March, A. R. & Morsut, L. Engineering multicellular systems: Using synthetic biology to control tissue self-organization. *Current Opinion in Biomedical Engineering* **4**, 163–173 (2017).
10. Kojima, R., Aubel, D. & Fussenegger, M. Building sophisticated sensors of extracellular cues that enable mammalian cells to work as “doctors” in the body. *Cellular and Molecular Life Sciences* (2020).
11. Shakiba, N., Jones, R. D., Weiss, R. & Vecchio, D. D. Context-aware synthetic biology by controller design: engineering the mammalian cell. *Cell Systems* **12**, 561–592 (2021).
12. Maze, A. & Benenson, Y. Artificial signaling in mammalian cells enabled by prokaryotic two-component system. *Nature Chemical Biology* **16**, 179–187 (2019).
13. Scheller, L. *et al.* Phosphoregulated orthogonal signal transduction in mammalian cells. *Nature Communications* **11**, 3085 (2020).
14. Capra, E. J., Perchuk, B. S., Skerker, J. M. & Laub, M. T. Adaptive mutations that prevent crosstalk enable the expansion of paralogous signaling protein families. *Cell* **150**, 222–232 (2012).

- 682 15. Galperin, M. Y. Structural classification of bacterial response regulators: Diversity of output domains and
683 domain combinations. *Journal of Bacteriology* **188**, 4169–4182 (2006).
- 684 16. Gao, R. & Stock, A. M. Biological Insights from Structures of Two-Component Proteins. *Annual Review of*
685 *Microbiology* **63**, 133–154 (2009).
- 686 17. Huynh, T. N. & Stewart, V. Negative control in two-component signal transduction by transmitter phosphatase
687 activity. *Molecular Microbiology* **82**, 275–286 (2011).
- 688 18. Jacob-Dubuisson, F., Mechaly, A., Betton, J. M. & Antoine, R. Structural insights into the signalling
689 mechanisms of two-component systems. *Nature Reviews Microbiology* **16**, 585–593 (2018).
- 690 19. Laub, M. T. & Goulian, M. Specificity in Two-Component Signal Transduction Pathways. *Annual Review of*
691 *Genetics* **41**, 121–145 (2007).
- 692 20. Siryaporn, A. & Goulian, M. Cross-talk suppression between the CpxA-CpxR and EnvZ-OmpR
693 two-component systems in *E. coli*. *Molecular Microbiology* **70**, 494–506 (2008).
- 694 21. Yang, Y. & Inouye, M. *Requirement of both kinase and phosphatase activities of an Escherichia coli receptor*
695 *(Taz1) for ligand-dependent signal transduction* 1993.
- 696 22. Hansen, J. *et al.* Transplantation of prokaryotic two-component signaling pathways into mammalian cells.
697 *PNAS* **111**, 15705–15710 (2014).
- 698 23. Goldbeter, A. & Koshland, D. E. An amplified sensitivity arising from covalent modification in biological
699 systems. *PNAS* **78**, 6840–6844 (1981).
- 700 24. Asthagiri, A. R. & Lauffenburger, D. A. A computational study of feedback effects on signal dynamics in a
701 mitogen-activated protein kinase (MAPK) pathway model. *Biotechnology Progress* **17**, 227–239 (2001).
- 702 25. Chang, Y. C., Armitage, J. P., Papachristodoulou, A. & Wadhams, G. H. A single phosphatase can convert a
703 robust step response into a graded, tunable or adaptive response. *Microbiology* **159**, 1276–1285 (2013).
- 704 26. Nilgiriwala, K. S., Jiménez, J., Rivera, P. M. & Del Vecchio, D. Synthetic Tunable Amplifying Buffer Circuit
705 in *E. coli*. *ACS Synthetic Biology* **4**, 577–584 (2015).
- 706 27. Qian, Y. & Del Vecchio, D. Realizing “Integral Control” In Living Cells: How To Overcome Leaky Integration
707 Due To Dilution? *Journal of The Royal Society Interface* **15**, 20170902 (2018).
- 708 28. Cai, S. J. & Inouye, M. EnvZ-OmpR interaction and osmoregulation in *Escherichia coli*. *Journal of Biological*
709 *Chemistry* **277**, 24155–24161 (2002).
- 710 29. Del Vecchio, D. Modularity, context-dependence, and insulation in engineered biological circuits. *Trends in*
711 *Biotechnology* **33**, 111–119 (2015).

- 712 30. Grunberg, T. W. & Del Vecchio, D. Modular Analysis and Design of Biological Circuits. *Current Opinion in*
713 *Biotechnology* **63**, 41–47 (2020).
- 714 31. Stock, A. M., Robinson, V. L. & Goudreau, P. N. Two-Component Signal Transduction. *Annual Review of*
715 *Biochemistry* **69**, 183–215 (2000).
- 716 32. Skarphol, K., Waukau, J. & Forst, S. A. Role of His243 in the phosphatase activity of EnvZ in Escherichia
717 coli. *Journal of Bacteriology* **179**, 1413–1416 (1997).
- 718 33. Hsing, W., Russo, F. D., Bernd, K. K. & Silhavy, T. J. Mutations that alter the kinase and phosphatase
719 activities of the two-component sensor EnvZ. *Journal of Bacteriology* **180**, 4538–4546 (1998).
- 720 34. Capra, E. J. *et al.* Systematic dissection and trajectory-scanning mutagenesis of the molecular interface that
721 ensures specificity of two-component signaling pathways. *PLoS Genetics* **6**, e1001220 (2010).
- 722 35. Park, H. & Inouye, M. Mutational analysis of the linker region of EnvZ, an osmosensor in Escherichia coli.
723 *Journal of Bacteriology* **179**, 4382–4390 (1997).
- 724 36. Zhu, Y., Qin, L., Yoshida, T. & Inouye, M. Phosphatase activity of histidine kinase EnvZ without kinase
725 catalytic domain. *PNAS* **97**, 7808–7813 (2000).
- 726 37. Qin, L., Dutta, R., Kurokawa, H., Ikura, M. & Inouye, M. A monomeric histidine kinase derived from EnvZ,
727 an Echerichia coli osmosensor. *Molecular Microbiology* **36**, 24–32 (2000).
- 728 38. Huynh, T. N., Noriega, C. E. & Stewart, V. Conserved mechanism for sensor phosphatase control of
729 two-component signaling revealed in the nitrate sensor NarX. *PNAS* **107**, 21140–5 (2010).
- 730 39. Willett, J. W. & Kirby, J. R. Genetic and Biochemical Dissection of a HisKA Domain Identifies Residues
731 Required Exclusively for Kinase and Phosphatase Activities. *PLoS Genetics* **8**, e1003084 (2012).
- 732 40. Wang, B., Zhao, A., Novick, R. P. & Muir, T. W. Activation and inhibition of the receptor histidine kinase
733 AgrC occurs through opposite helical transduction motions. *Molecular Cell* **53**, 929–940 (2014).
- 734 41. Ashenberg, O., Rozen-Gagnon, K., Laub, M. T. & Keating, A. E. Determinants of homodimerization
735 specificity in histidine kinases. *Journal of Molecular Biology* **413**, 222–235 (2011).
- 736 42. Egger, L. a., Park, H. & Inouye, M. Signal transduction via the histidyl-aspartyl phosphorelay. *Genes to Cells*
737 **2**, 167–184 (1997).
- 738 43. Hardman, G. *et al.* Strong anion exchange-mediated phosphoproteomics reveals extensive human
739 non-canonical phosphorylation. *The EMBO Journal* **38**, 1–22 (2019).
- 740 44. Gam, J. J., DiAndreth, B., Jones, R. D., Huh, J. & Weiss, R. A 'poly-transfection' method for rapid, one-pot
741 characterization and optimization of genetic systems. *Nucleic Acids Research* **47**, e106 (2019).

- 742 45. Iwamoto, M., Björklund, T., Lundberg, C., Kirik, D. & Wandless, T. J. A general chemical method to regulate
743 protein stability in the mammalian central nervous system. *Chemistry and Biology* **17**, 981–988 (2010).
- 744 46. Miyazaki, Y., Imoto, H., Chen, L. & Wandless, T. Destabilizing domains derived from the human estrogen
745 receptor. *Journal of the American Chemical Society* **134**, 3942–3945 (2012).
- 746 47. Landgraf, P. *et al.* A Mammalian microRNA Expression Atlas Based on Small RNA Library Sequencing. *Cell*
747 **129**, 1401–1414 (2007).
- 748 48. Xie, Z., Wroblewska, L., Prochazka, L., Weiss, R. & Benenson, Y. Multi-Input RNAi-Based Logic Circuit for
749 Identification of Specific Cancer Cells. *Science* **333**, 1307–1311 (2011).
- 750 49. Rinaudo, K. *et al.* A universal RNAi-based logic evaluator that operates in mammalian cells. *Nature*
751 *Biotechnology* **25**, 795–801. arXiv: arXiv:1011.1669v3 (2007).
- 752 50. Head, C. G., Tardy, A. & Kenney, L. J. Relative binding affinities of OmpR and OmpR-phosphate at the ompF
753 and ompC regulatory sites. *Journal of Molecular Biology* **281**, 857–870 (1998).
- 754 51. Jones, R. D. *et al.* An endoribonuclease-based feedforward controller for decoupling resource-limited genetic
755 modules in mammalian cells. *Nature Communications*, 5690 (2020).
- 756 52. Raj, A., Peskin, C. S., Tranchina, D., Vargas, D. Y. & Tyagi, S. Stochastic mRNA synthesis in mammalian
757 cells. *PLoS Biology* **4**, 1707–1719 (2006).
- 758 53. Gutierrez, P. S., Monteoliva, D. & Diambra, L. Cooperative Binding of Transcription Factors Promotes
759 Bimodal Gene Expression Response. *PLoS ONE* **7** (2012).
- 760 54. Meyer, A. J., Segall-Shapiro, T. H., Glassey, E., Zhang, J. & Voigt, C. A. Escherichia coli “Marionette” strains
761 with 12 highly optimized small-molecule sensors. *Nature Chemical Biology* **15**, 196–204 (2019).
- 762 55. Qian, Y., Huang, H. H., Jiménez, J. I. & Del Vecchio, D. Resource Competition Shapes the Response of
763 Genetic Circuits. *ACS Synthetic Biology* **6** (2017).
- 764 56. Frei, T. *et al.* Characterization and mitigation of gene expression burden in mammalian cells. *Nature*
765 *Communications* **11**, 4641 (2020).
- 766 57. Sturm, O. E. *et al.* The mammalian MAPK/ERK pathway exhibits properties of a negative feedback amplifier.
767 *Science Signaling* **3**, ra90 (2010).
- 768 58. Nevozhay, D., Adams, R. M., Murphy, K. F., Josic, K. & Balazsi, G. Negative autoregulation linearizes the
769 dose-response and suppresses the heterogeneity of gene expression. *PNAS* **106**, 5123–5128. arXiv:
770 arXiv:1408.1149 (2009).
- 771 59. Siciliano, V. *et al.* MiRNAs confer phenotypic robustness to gene networks by suppressing biological noise.
772 *en. Nature Communications* **4**, 2364 (Jan. 2013).

- 773 60. Huang, H.-H., Qian, Y. & Del Vecchio, D. A quasi-integral controller for adaptation of genetic modules to
774 variable ribosome demand. *Nature Communications* **9**, 5415 (2018).
- 775 61. Aoki, S. K. *et al.* A universal rationally-designed biomolecular integral feedback controller for robust perfect
776 adaptation. *Nature* **570**, 533–537 (2019).
- 777 62. Ng, A. H. *et al.* Modular and tunable biological feedback control using a de novo protein switch. *Nature* **572**,
778 265–269 (2019).
- 779 63. Szymczak, A. L. *et al.* Correction of multi-gene deficiency in vivo using a single 'self-cleaving' 2A
780 peptide-based retroviral vector. *Nature Biotechnology* **22**, 589–594 (2004).
- 781 64. Berger, S. L., Cress, W., Cress, A., Triezenberg, S. J. & Guarente, L. Selective inhibition of activated but not
782 basal transcription by the acidic activation domain of VP16: Evidence for transcriptional adaptors. English.
783 *Cell* **61**, 1199–1208 (June 1990).
- 784 65. Schmidl, S. R. *et al.* Rewiring bacterial two-component systems by modular DNA-binding domain swapping.
785 *Nature Chemical Biology* **15**, 690–698 (2019).
- 786 66. Muldoon, J. J. *et al.* Model-guided design of mammalian genetic programs. *Science Advances* **7**, eabe9375
787 (2021).
- 788 67. Samaniego, C. C., Moorman, A., Giordano, G. & Franco, E. Signaling-based neural networks for cellular
789 computation, Preprint at <https://www.biorxiv.org/content/10.1101/2020.11.10.377077v1> (2020).
- 790 68. Cuba Samaniego, C. & Franco, E. Ultrasensitive molecular controllers for quasi-integral feedback. *Cell*
791 *Systems* **12**, 272–288 (2021).
- 792 69. Del Vecchio, D., Ninfa, A. J. & Sontag, E. D. Modular cell biology: retroactivity and insulation. *Molecular*
793 *Systems Biology* **4**, 161 (2008).
- 794 70. Jayanthi, S. & Del Vecchio, D. Retroactivity attenuation in bio-molecular systems based on timescale
795 separation. *IEEE Transactions on Automatic Control* **56**, 748–761 (2011).
- 796 71. Mishra, D., Rivera, P. M., Lin, A., Del Vecchio, D. & Weiss, R. A load driver device for engineering
797 modularity in biological networks. *Nature Biotechnology* **32**, 1268–75 (2014).
- 798 72. Yamamoto, K. & Ishihama, A. Transcriptional response of Escherichia coli to external zinc. *Journal of*
799 *Bacteriology* **187**, 6333–6340 (2005).
- 800 73. Procaccini, A., Lunt, B., Szurmant, H., Hwa, T. & Weigt, M. Dissecting the specificity of protein-protein
801 interaction in bacterial two-component signaling: Orphans and crosstalks. *PLoS ONE* **6** (2011).
- 802 74. Willett, J. W. *et al.* Specificity residues determine binding affinity for two-component signal transduction
803 systems. *mBio* **4**, 1–11 (2013).

- 804 75. McClune, C. J., Alvarez-Buylla, A., Voigt, C. A. & Laub, M. T. Engineering orthogonal signalling pathways
805 reveals the sparse occupancy of sequence space. *Nature* **574**, 702–706 (2019).
- 806 76. Yi, T.-M., Huang, Y., Simon, M. I. & Doyle, J. Robust perfect adaptation in bacterial chemotaxis through
807 integral feedback control. *PNAS* **97**, 4649–4653 (Apr. 2000).
- 808 77. Rosenfeld, N., Elowitz, M. B. & Alon, U. Negative Autoregulation Speeds the Response Times of
809 Transcription Networks. **323**, 785–793 (Nov. 2002).
- 810 78. Olsman, N. *et al.* Hard Limits and Performance Tradeoffs in a Class of Antithetic Integral Feedback Networks.
811 *Cell Systems* **9**, 49–63.e16 (2019).
- 812 79. Åström, K. J. & Murray, R. M. *Feedback systems: an introduction for scientists and engineers* (Princeton
813 University Press, 2008).
- 814 80. Groisman, E. A. Feedback Control of Two-Component Regulatory Systems. *Annual Review of Microbiology*
815 **70**, 103–124 (2016).
- 816 81. Yeo, W. S. *et al.* Intrinsic Negative Feedback Governs Activation Surge in Two-Component Regulatory
817 Systems. *Molecular Cell* **45**, 409–421 (2012).
- 818 82. Alon, U., Surette, M. G., Barkai, N. & Leibler, S. Robustness in bacterial chemotaxis. *Nature* **397**, 168–171
819 (Jan. 1999).
- 820 83. Lake, D., Corrêa, S. A. L. & Müller, J. Negative feedback regulation of the ERK1/2 MAPK pathway. *Cellular*
821 *and Molecular Life Sciences* **73**, 4397–4413 (2016).
- 822 84. Yoon, S. & Seger, R. The extracellular signal-regulated kinase: Multiple substrates regulate diverse cellular
823 functions. *Growth Factors* **24**, 21–44 (2006).
- 824 85. McKay, M. M. & Morrison, D. K. Integrating signals from RTKs to ERK/MAPK. *Oncogene* **26**, 3113–3121
825 (2007).
- 826 86. Caunt, C. J. & Keyse, S. M. Dual-specificity MAP kinase phosphatases (MKPs): Shaping the outcome of
827 MAP kinase signalling. *FEBS Journal* **280**, 489–504 (2013).
- 828 87. Fritsche-Guenther, R. *et al.* Strong negative feedback from Erk to Raf confers robustness to MAPK signalling.
829 *Molecular Systems Biology* **7**, 489 (2011).
- 830 88. Nunns, H. & Goentoro, L. Signaling pathways as linear transmitters. *eLife* **7**, 1–37 (2018).
- 831 89. Salmond, R. J., Brownlie, R. J., Morrison, V. L. & Zamoyska, R. The tyrosine phosphatase PTPN22
832 discriminates weak self peptides from strong agonist TCR signals. *Nature Immunology* **15**, 875–883 (2014).

- 833 90. Li, Q. J. *et al.* miR-181a Is an Intrinsic Modulator of T Cell Sensitivity and Selection. *Cell* **129**, 147–161
834 (2007).
- 835 91. Gaud, G., Lesourne, R. & Love, P. E. Regulatory mechanisms in T cell receptor signalling. *Nature Reviews*
836 *Immunology* **18**, 485–497 (2018).
- 837 92. Rodríguez-Galán, A., Fernández-Messina, L. & Sánchez-Madrid, F. Control of immunoregulatory molecules
838 by miRNAs in T cell activation. *Frontiers in Immunology* **9**, 2148 (2018).
- 839 93. Duportet, X. *et al.* A platform for rapid prototyping of synthetic gene networks in mammalian cells. *Nucleic*
840 *Acids Research* **42**, 13440–13451 (Nov. 2014).
- 841 94. Sandelin, A. *et al.* Mammalian RNA polymerase II core promoters: insights from genome-wide studies.
842 *Nature Reviews Genetics* **8**, 424–436 (2007).
- 843 95. Roy, A. L. & Singer, D. S. Core promoters in transcription: Old problem, new insights. *Trends in Biochemical*
844 *Sciences* **40**, 165–171 (2015).
- 845 96. Haberle, V. & Stark, A. Eukaryotic core promoters and the functional basis of transcription initiation. *Nature*
846 *Reviews Molecular Cell Biology* **19**, 621–637 (2018).
- 847 97. Ede, C., Chen, X., Lin, M. Y. & Chen, Y. Y. Quantitative Analyses of Core Promoters Enable Precise
848 Engineering of Regulated Gene Expression in Mammalian Cells. *ACS Synthetic Biology* **5**, 395–404 (2016).
- 849 98. Ponjavic, J. *et al.* Transcriptional and structural impact of TATA-initiation site spacing in mammalian core
850 promoters. *Genome biology* **7**, R78 (2006).
- 851 99. Gao, R., Mack, T. R. & Stock, A. M. Bacterial response regulators: versatile regulatory strategies from
852 common domains. *Trends in Biochemical Sciences* **32**, 225–234 (2007).

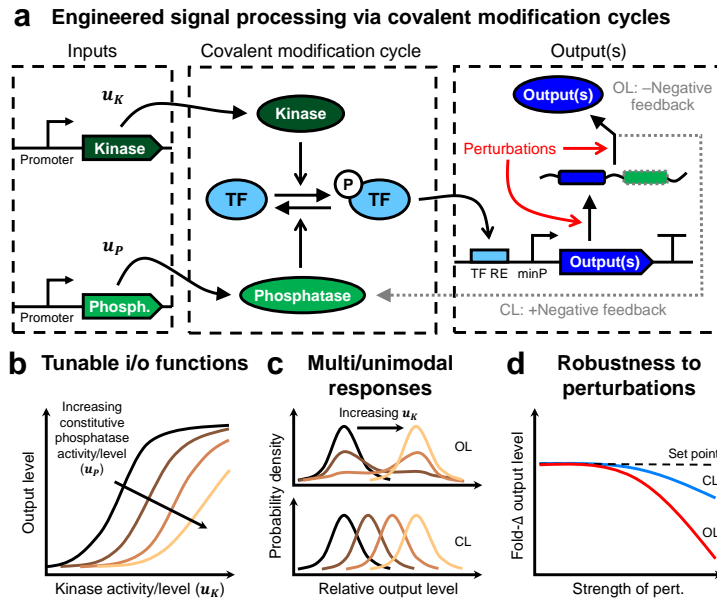
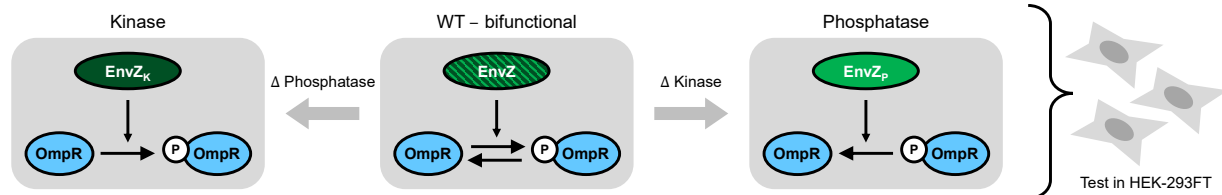
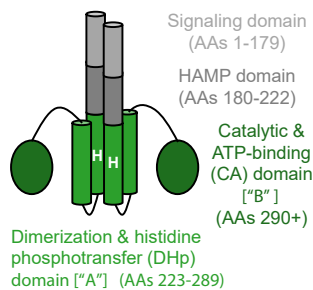


Figure 1

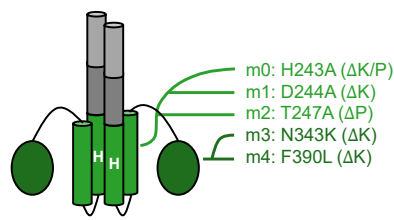
a Strategy for generating TF-specific kinases and phosphatases



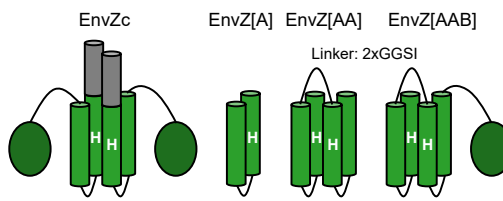
b EnvZ dimer structure



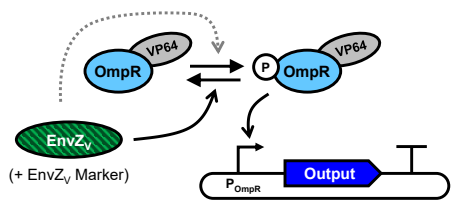
c EnvZ mutants



d EnvZ truncations/rearrangements



e Assay for kinase activity



f Assay for phosphatase activity

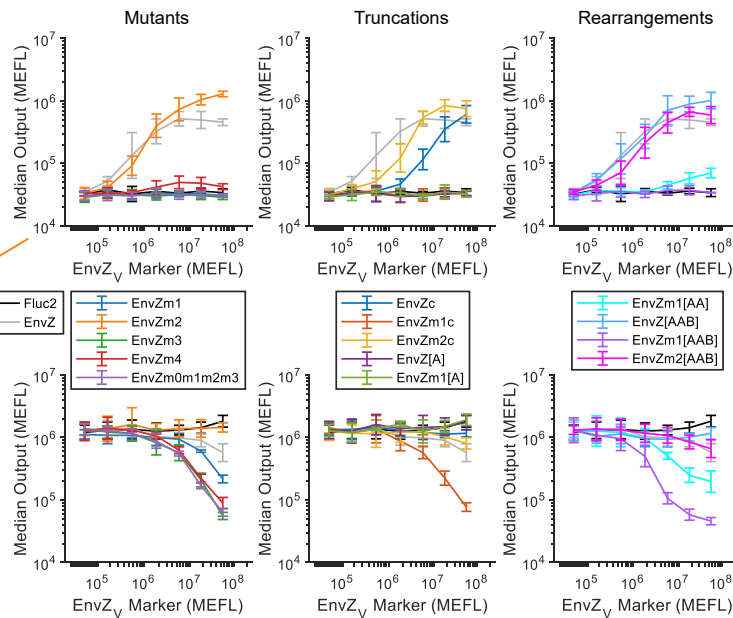
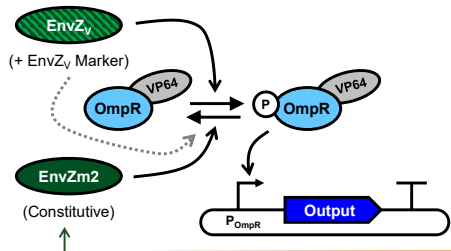
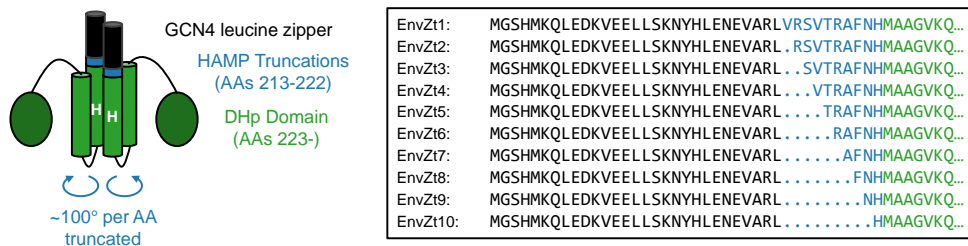
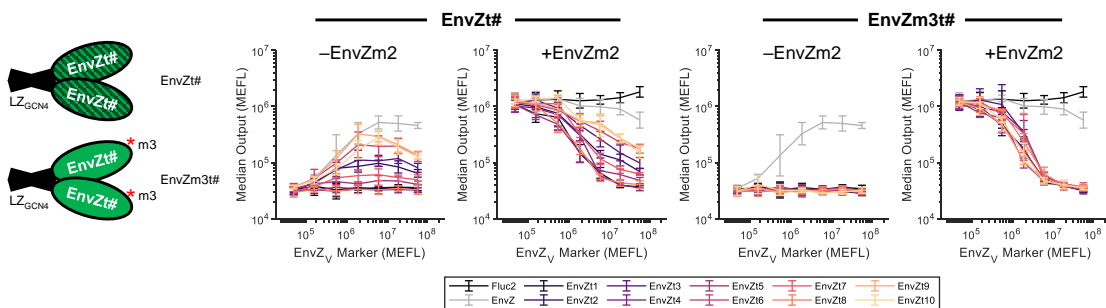


Figure 2

a Tuning enzyme activity through DHp domain rotations



b Kinase and phosphatase activity assays



c Angular mapping of enzymatic activities

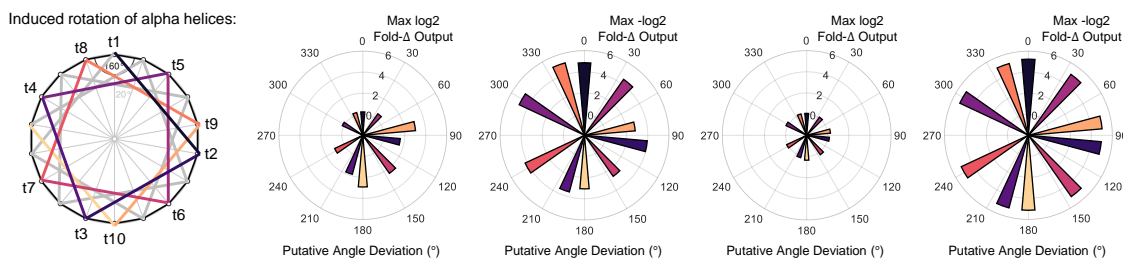
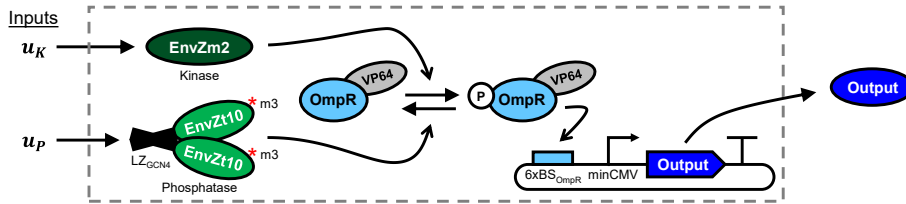
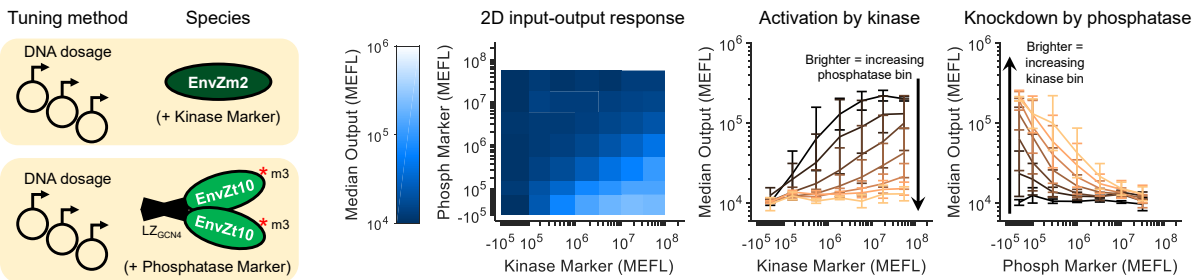


Figure 3

a Tunable genetic device based on covalent modification cycles



b Tunable i/o responses



c Small molecule-tuned i/o responses

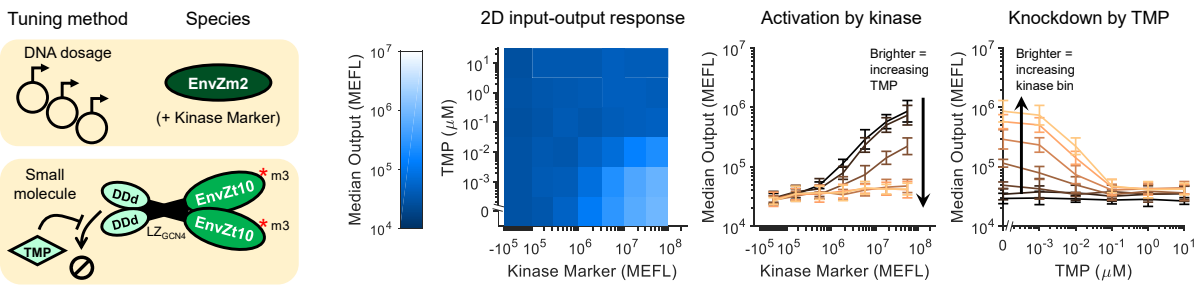


Figure 4

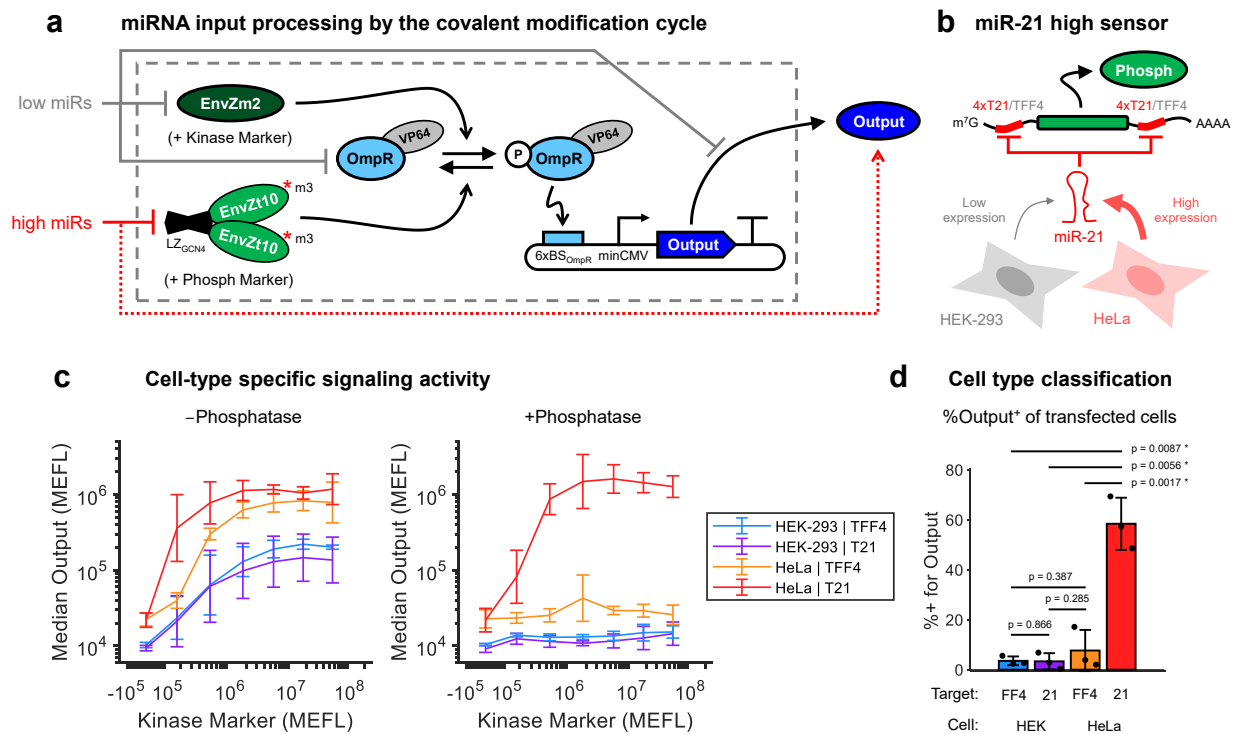
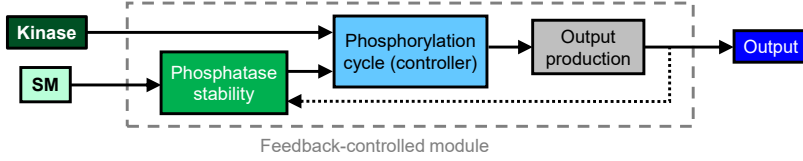
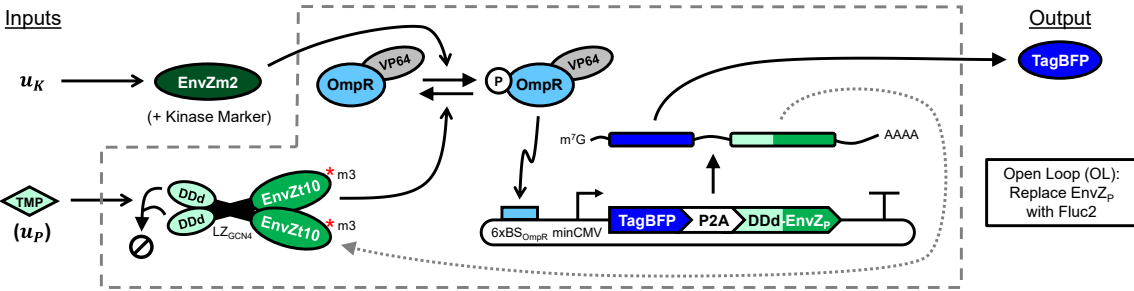


Figure 5

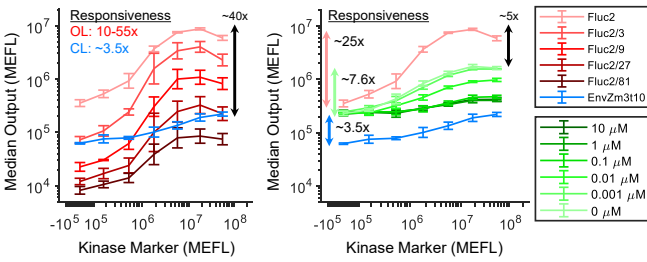
a Phosphorylation-based feedback controller design



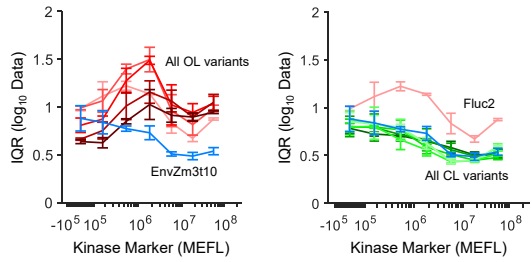
b Feedback controller implementation



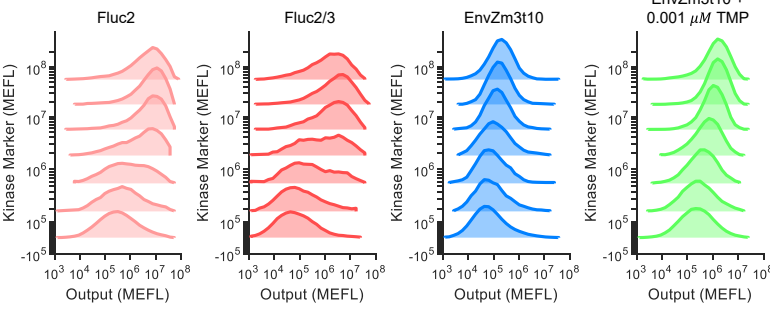
c Kinase-output dose responses



d Output noise per kinase dosage



e Output distributions per kinase dosage



f Noise per level of output

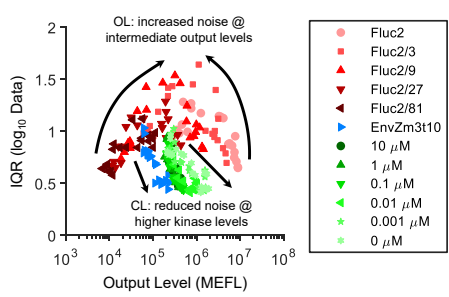
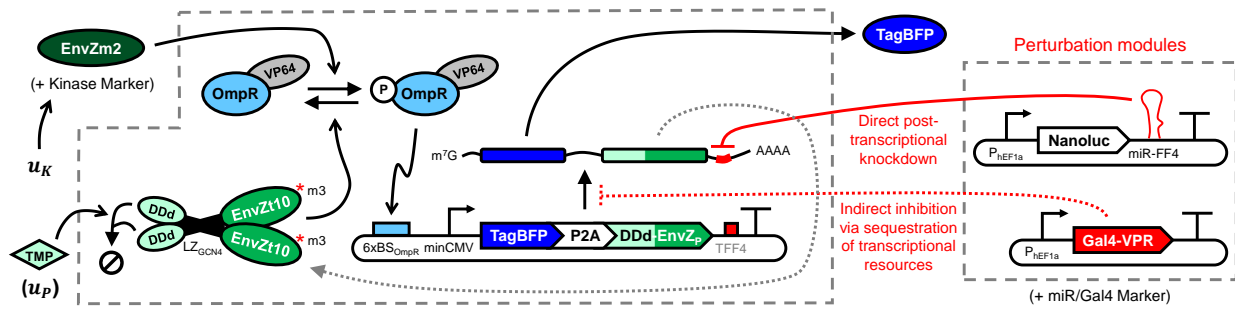
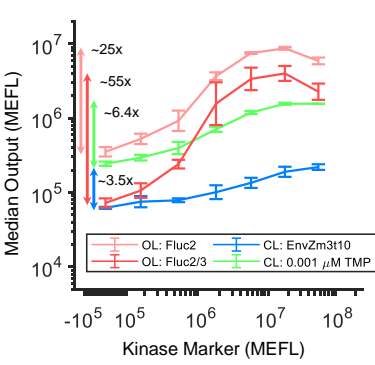


Figure 6

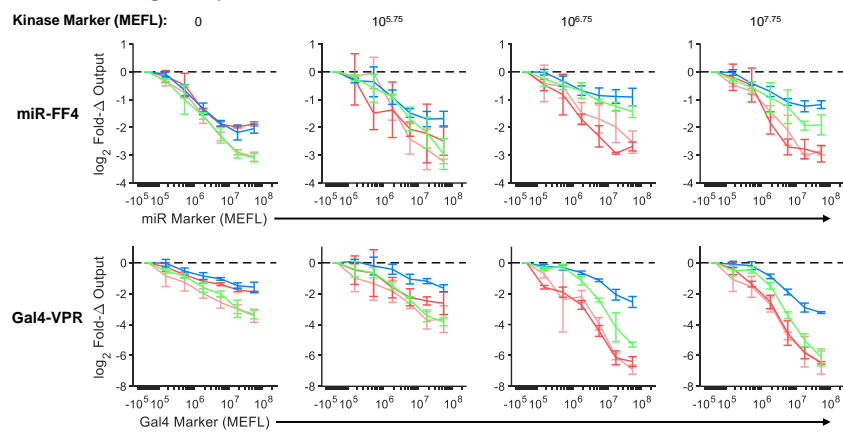
a System for testing response of feedback controller to perturbations



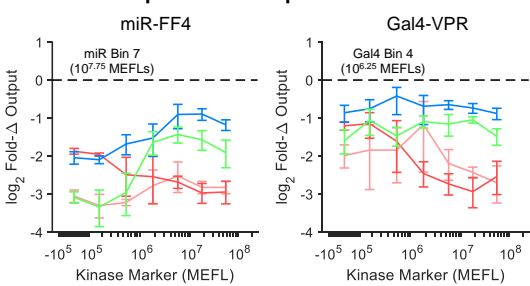
b Kinase-output dose responses of highlighted OL and CL variants



c Fold-changes to perturbations



d Effects of perturbations per kinase level



e Robustness at comparable output levels

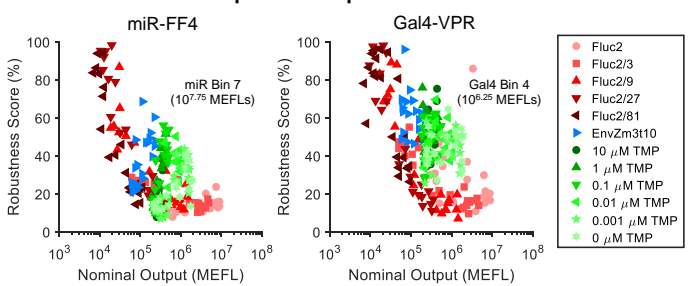


Figure 7

854 Figure Legends

855 **Figure 1. Overview of engineered covalent modification cycle.** (a) A covalent modification cycle (CMC) is

856 composed of a substrate that is interconverted between an active and an inactive form by two different enzymes. Here
857 we examine a CMC created by reversible phosphorylation/dephosphorylation of a transcription factor (TF) by a
858 kinase and phosphatase. The inputs to this CMC, u_K and u_P , alter the production rate or catalytic rates of the kinase
859 and phosphatase, respectively. The output(s) of the system are RNA and/or protein species, whose production is
860 activated by the TF when phosphorylated. Closed loop (CL) negative feedback control can be achieved by
861 co-expressing a phosphatase with the output. Without the feedback, the expression of the outputs is open loop (OL).
862 (b) The input/output (i/o) response of the system, *i.e.* the response of the TF-driven output(s) to kinase inputs (u_K),
863 can be tuned via phosphatase inputs (u_P). Brighter lines correspond to increasing concentration or activity of the
864 phosphatase. (c) Negative feedback is expected to convert multimodal output responses into unimodal responses.
865 Here, brighter lines correspond to increasing kinase concentration/activity. (d) Negative feedback is expected to
866 impart robustness to perturbations in the output production process. The set point refers to the level of output in the
867 absence of a perturbation.

868 **Figure 2. Engineering the bifunctional histidine kinase EnvZ to isolate kinase and phosphatase activities.**

869 (a) Model system to construct a covalent modification cycle (CMC): EnvZ/OmpR proteins from *E. coli*

870 two-component signaling (TCS). EnvZ naturally exhibits both kinase and phosphatase activities. By mutating or
871 changing the enzyme structure, either one or the other activity is eliminated to yield a kinase or a phosphatase

872 specific for OmpR. (b) Schematic of EnvZ. In *E. coli*, the signaling domain senses increasing environmental
873 osmolarity, which is transmuted via the HAMP domain to the rest of the structure. Upon receiving this input signal,
874 the CA domain ["B"] binds to ATP and autophosphorylates a conserved histidine residue in the DHp domain ["A"].

875 This phosphate group is then transferred to the cognate response regulator, OmpR. In the absence of signal input, the
876 DHp domain catalyzes dephosphorylation of OmpR. In mammalian cells, wild-type EnvZ is constitutively active²².

877 (c) Mutants of EnvZ^{32-34,39,100} tested in this study, mapped onto their location in the EnvZ structure. (d)

878 Truncations^{35,36} and domain rearrangements³⁷ of EnvZ tested in this study. (e) Evaluation of EnvZ variants for
879 improved kinase activity. Constitutively-expressed OmpR-VP64 (OmpR fused to the activation domain VP64) was
880 co-transfected with a reporter plasmid comprising a promoter (P_{OmpR}) with 6xOmpR binding sites and a minimal
881 CMV promoter driving TagBFP as the output. Each EnvZ variant ($EnvZ_V$) was co-delivered with $EnvZ_V$ Marker, a
882 fluorescent reporter that indicates dosage per cell, and poly-transfected against the other plasmids to evaluate the
883 $EnvZ_V$ -to-output dose-responses (see Supplementary Figure 2 for additional details). The solid arrow from $EnvZ_V$ to
884 the phosphorylation cycle indicates the desired kinase activity, while the dashed arrow indicates the possibility of

885 residual phosphatase activity. The plots on the right show the expression of OmpR-driven TagBFP (Output) in
886 response to increasing EnvZ_V dosages, as measured by EnvZ_V Marker. (f) Evaluation of EnvZ variants for
887 phosphatase activity. The experiment is similar to Panel (e), except that the variant EnvZm2, which has a strong
888 kinase bias, is constitutively expressed to set a baseline level of OmpR phosphorylation. The solid and dashed arrows
889 are swapped to indicate the desire for phosphatase activity and possibility of residual kinase activity. All data in
890 panels (e) and (f) were measured by flow cytometry at 48 hours post-transfection in HEK-293FT cells. All errorbars
891 represent the mean ± s.d. of measurements from three experimental repeats.

892 **Figure 3. Fixing DHP domain rotation to tune kinase activity and isolate strong phosphatases.** (a) Fusion of
893 GCN4 leucine zipper to the N-terminus of EnvZ truncated between residues 212 and 221, thus connecting to the DHP
894 domain and fixing the rotation of its alpha helices⁴⁰. The box on the right shows the sequence of the first 37-46 amino
895 acids of each variant. (b) Kinase and phosphatase activity assays for each rotationally-locked variant (same
896 experiment design as in Figure 2e-f). EnvZm2, a kinase-biased variant, establishes a baseline of phosphorylated
897 OmpR for testing dephosphorylation. EnvZm3t# have mutation 'm3' (N343K), which knocks out kinase activity. (c)
898 Maximum fold-change in output expression induced by each variant mapped to the putative rotational conformation
899 of the DHP domain, assuming 100° of rotation for each amino acid truncated between GCN4 and the DHP domain
900 and setting EnvZt1 to 0°. All data were measured by flow cytometry at 48 hours post-transfection in HEK-293FT
901 cells. All errorbars represent the mean ± s.d. of measurements from three experimental repeats.

902 **Figure 4. Tuning input/output signaling response by modulating kinase and phosphatase levels.** (a)
903 Implementation of a covalent modification cycle with kinase (EnvZm2) and phosphatase (EnvZm3t10) variants of
904 EnvZ. The expression level of the output can be tuned as a function of both enzymes, and inputs to each that affect
905 their production rate (u_K and u_P). (b) Tuning output expression through different dosages of kinase and phosphatase
906 DNA. The heatmap shows the median level of output for each combination of kinase and phosphatase DNA dosages,
907 assayed with poly-transfection⁴⁴ (see Supplementary Figure 14 for full data). The line plots show the same data but
908 broken out by rows or columns. Brighter lines correspond to bins with increasing phosphatase (left) or kinase (right).
909 (c) Tuning output expression through small molecule-induced degradation of the phosphatase. DDd is fused to the
910 N-terminus of the phosphatase (see Supplementary Figure 10 for different arrangements and comparison with
911 DDe/4-OHT). Addition of TMP stabilizes the DDd-phosphatase fusion protein⁴⁵. The data is extracted from the full
912 poly-transfection results shown in Supplementary Figures 10 & 11, selecting the middle phosphatase bin (P Marker
913 ≈ 10⁶). The line plots show the same data but broken out by rows or columns. Brighter lines correspond to samples
914 with increasing TMP concentration (left) or bins with increasing kinase (right). All data were measured by flow

915 cytometry at 48 hours post-transfection. HEK-293 cells were used for Panel (b) and HEK-293FT for Panel (c). All
916 errorbars represent the mean \pm s.d. of measurements from three experimental repeats. All heatmap values represent
917 the mean of measurements from three experimental repeats.

918 **Figure 5. Cell type-specific signaling responses using covalent modification cycles. (a)** miRNA classifier
919 design based on covalent modification cycles. miRNAs expected to be low in the target cell can be used to knock
920 down the kinase, OmpR-VP64, and/or the output. miRNAs expected to be high in the target cell can be used to knock
921 down the phosphatase, effectively increasing the output expression. Not shown for brevity, the level of OmpR-VP64
922 was optimized using a feedforward controller (Supplementary Figure 12). **(b)** Design of a miR-21 sensor for
923 classification of HeLa cells. miR-21 knocks down phosphatase levels via 4x target sites in each of its 5' and 3'
924 untranslated regions (UTRs). As a control, a variant was made with miR-FF4 target sites (TFF4) in place of the
925 miR-21 target sites (T21), thus preventing knockdown by miR-21. miR-21 is differentially expressed in HeLa
926 compared to HEK-293 cells^{44,48}. **(c)** Cell type-specific signaling responses enabled by miRNA regulation of
927 phosphatase expression. The data is extracted from the full poly-transfection data (Supplementary Figure 14),
928 comparing the second-highest phosphatase bin (P Marker $\approx 10^7$) to the lowest (no phosphatase). **(d)** Comparison of
929 the percent of transfected cells positive for the output for each circuit variant in HEK/HeLa cells. P-values are from
930 two-tailed paired T-tests between each group of samples. Receiver-operator characteristic (ROC) curves are provided
931 in Supplementary Figures 16 & 17. All data were measured by flow cytometry at 48 hours post-transfection. All
932 errorbars represent the mean \pm s.d. of measurements from three experimental repeats.

933 **Figure 6. Design and implementation of a tunable phosphorylation-based feedback controller. (a)** Block
934 diagram of the feedback controller design. The phosphatase acts as an output sensor, and is fed back from the output
935 to the phosphorylation cycle of the TF that activates output production. The kinase sets the reference for output
936 expression. The output responds to inputs both to the kinase and a small molecule (SM) regulator of phosphatase
937 stability, the latter effectively serving to tune the feedback strength. **(b)** Implementation of the feedback controller.
938 the kinase is EnvZm2, the phosphatase is DDd-EnvZm3t10, and the output is the fluorescent reporter TagBFP, and
939 the output is 2A-linked⁶³ to the phosphatase to ensure coupled transcription. Addition of TMP stabilizes
940 DDd-EnvZm3t10 and thereby increases the feedback strength. An open loop (OL) version of the system was made
941 by replacing the phosphatase with the luminescent protein Fluc2. Since negative feedback reduces output expression,
942 OL variants with reduced output level were created for comparison at equivalent output levels by reducing the copy
943 number of output reporter by fractional amounts (1:3, 1:9, 1:27, and 1:81). The kinase was poly-transfected in a
944 separate complex to the other plasmids to measure the dose-responses of the OL and closed loop (CL) systems (see

945 Supplementary Figures 19 for details). (c) Dose-responses of OL and CL system outputs to kinase input levels. The
946 range of responsiveness to kinase (max fold change \pm kinase) are given for the CL and OL variants are indicated to
947 the left of the lines. The fold-difference between max output levels for select OL and CL variants are indicated to the
948 right of the lines. Dose-responses of the DDd-CL system are given in Supplementary Figure 24. (d) Quantification of
949 output noise as a function of kinase input dosages. Because the output variance is log-distributed, the interquartile
950 range (IQR) is computed on the log-transformed data. (e) Comparison of output distributions for select OL and CL
951 variants across kinase levels. The data is representative from the first experimental repeat. All OL and CL variants are
952 compared in Supplementary Figure 23. (f) Noise as a function of median output levels for all CL and OL variants at
953 all kinase inputs. The individual points are drawn from all experimental repeats. All data were measured by flow
954 cytometry at 48 hours post-transfection in HEK-293FT cells. All errorbars represent the mean \pm standard deviation
955 of measurements from three experimental repeats.

956 **Figure 7. Mitigation of perturbations via feedback control.** (a) The CL and OL systems introduced in Figure 6
957 were tested against two perturbations: (i) indirect transcriptional inhibition via loading of transcriptional resource by
958 Gal4-VPR and (ii) direct post-transcriptional knockdown by miR-FF4. The kinase, perturbations, and controllers
959 were each poly-transfected in separate DNA-lipid complexes in order to measure the 2D dose-response of the OL and
960 CL systems to the kinase and perturbations (see Supplementary Figures 19-22 for details). (b) Dose-responses of OL
961 and CL systems highlighted in the following panels. The Fluc2 and Fluc2/3 OL variants were chosen since they have
962 nearly identical output levels compared to the CL with and without DDd, respectively, in the absence of kinase.
963 Dose-responses and detailed comparisons among all OL and CL variants are provided in Supplementary Figures
964 25-28. (c) Fold-changes (Fold- Δ s) in output expression in response to miR-FF4 (top row) and Gal4-VPR (bottom
965 row) perturbations. Each column represents an increasing amount of kinase input from left to right. The dashed lines
966 indicate no fold-change (ideal). (d) Direct comparison of fold-changes to perturbations between OL and CL variants
967 across kinase dosages. The data represents the maximum dosage of miR-FF4 (miR Marker $\approx 10^{7.75}$ MEFLs) and a
968 dosage of Gal4-VPR with a comparable level of knockdown to the OL (Gal4 Marker $\approx 10^{6.25}$ MEFLs). (f)
969 Robustness scores (100% - % deviation due to perturbations) for all OL and CL variants across each kinase input
970 level at the same dosages of miR-FF4 and Gal4-VPR as highlighted in Panel (d). Nominal outputs indicate the level
971 of output in the absence of any perturbations. The individual points are drawn from all experimental repeats. All data
972 were measured by flow cytometry at 48 hours post-transfection in HEK-293FT cells. All errorbars represent the
973 mean \pm standard deviation of measurements from three experimental repeats.